colloids and interfaces

MDPI

Review

Two-Dimensional Materials for Selective Ion Transport Membrane: Synthesis and Application Advances

Zhijian Jiang [1], Shining Zhang [1], Jianzhi Xu [1], Ying Liu [1], Yuanyuan Zhang [2,3,*], Jianguo Liu [1,*] and Zicheng Zuo [1,*]

[1] Institute of Energy Power Innovation, North China Electric Power University, Beijing 102206, China; jianzhi0808@163.com (Z.J.); 14794439637@163.com (S.Z.); xjz0301@foxmail.com (J.X.); alyytu@163.com (Y.L.)
[2] Research Center for Eco-Environmental Sciences, Chinese Academy of Sciences, Beijing 100085, China
[3] University of Chinese Academy of Sciences, Beijing 100049, China
* Correspondence: yyzhang@rcees.ac.cn (Y.Z.); jianguoliu@ncepu.edu.cn (J.L.); zuozic@ncepu.edu.cn (Z.Z.)

Abstract

Membrane innovations have become a key solution for overcoming the bottlenecks in efficiency upgrade in many green energy fields. Membrane performance depends on two key parameters permeability and selectivity, which typically follow a trade-off relationship: improving one often diminishes the other. Two-dimensional (2D) materials, which have atomic-level thickness, tunable pore sizes, and reasonable functionalization, offer great promises to break through the trade-off effect and redesign high-efficiency mass transfer pathways. This review systematically presents recent efforts in both preparation and potential applications of 2D materials for overcoming the permeability–selectivity trade-off. It highlights four prevailing fabrication strategies: chemical vapor deposition, interfacial synthesis, solution-phase synthesis, and exfoliation, and shows some major optimization techniques for various 2D materials. Additionally, this review discusses emerging applications of 2D materials across critical fields from water treatment (seawater desalination, metal ion extraction) to energy technologies (osmotic power generation, direct methanol fuel cells, and vanadium redox flow batteries). Finally, the challenges and future prospects of 2D materials in ion separation and energy conversion are discussed.

Keywords: 2D Material; ion permeability; selectivity; trade-off effect; membrane separation

check for updates

Academic Editor: Rajinder Pal

Received: 15 August 2025
Revised: 6 September 2025
Accepted: 12 September 2025
Published: 17 September 2025

Citation: Jiang, Z.; Zhang, S.; Xu, J.; Liu, Y.; Zhang, Y.; Liu, J.; Zuo, Z. Two-Dimensional Materials for Selective Ion Transport Membrane: Synthesis and Application Advances. *Colloids Interfaces* **2025**, *9*, 63. https://doi.org/10.3390/colloids9050063

Copyright: © 2025 by the authors. Licensee MDPI, Basel, Switzerland. This article is an open access article distributed under the terms and conditions of the Creative Commons Attribution (CC BY) license (https://creativecommons.org/licenses/by/4.0/).

1. Introduction

Towards carbon neutrality, promoting energy efficiency in both energy-production and energy-consumption industries becomes significant to solve the challenges in satisfying the explosive growth of the energy demand [1]. Ion-selective membrane materials are one of the most crucial components for many sustainable technologies, including water treatment and energy conversion devices [2,3]. However, the trade-off between permeability and selectivity is one of the main scientific issues that remarkably prevents the transformative performance of these corresponding devices. Breaking the trade-off effect faces substantial bottlenecks, because angstrom-level perforation with precise high-flux ion selectivity is still far from attainable with existing techniques and the ion hydration further complicates the diffusion. Ion selectivity is primarily determined by two key membrane characteristics: (1) the precise pore size distribution and (2) electrostatic interactions arising from functional groups [4,5]. Conventional polymeric membranes typically possess tortuous transport pathways with inhomogeneous channel sizes, resulting in an inherent trade-off between permeability and selectivity [6].

Over the past two decades, significant advancements have been made in material synthesis methodologies. Emerging materials such as metal–organic frameworks (MOFs) [7], covalent organic frameworks (COFs) [8], carbon-based materials (e.g., graphene and graphdiyne) [9–11], MXenes [12], and layered double hydroxides (LDHs) [13] have become prominent research frontiers in membrane science. The rapid development in membrane chemistry has laid the foundation for precise control over pore dimensions and channel functionality [14,15]. It has established new paradigms for constructing confined transport environments, developing innovative transport mechanisms, and ultimately overcoming the pervasive trade-off effect between permeability and selectivity [16,17].

Among these materials, atomically thin 2D materials represent as an ideal platform for challenging the trade-off effect and have received intensive attention [18,19]. Its atomic-level thickness and precisely controllable nanochannels are primarily responsible for its ability to achieve rapid and precise ion screening [20]. According to the Nernst–Planck equation, 2D membrane materials possibly enable minimized diffusion distances and energy barriers while simultaneously maximizing concentration gradients (diffusion) and electric potential gradients [21,22], thereby enhancing ion flux [23,24]. Currently, two main mass transfer mechanisms have been developed based on the 2D membrane materials (Figure 1). One is ion in-plane transport [25,26], and the other is interlayer channel transport [27]. In-plane transport mechanism utilizes either intrinsic in-plane pores or engineered defects within 2D materials for selective ion conduction. Target ions can possibly transport the membrane through the shortest pathways, and this approach holds the greatest potential for achieving minimal energy barrier transport—making it the most desirable configuration for researchers. However, the key challenges lie in fabricating angstrom-level pores with optimal ion selectivity and permeability and increasing pore areal density while maintaining precision [28]. For the other one, the ions transport through the interlayer in the laminated membrane. The ion selectivity heavily relies on the regulation efficiency of interlayer van der Waals interactions. Such ion transport behavior predominantly occurs in lamellar membranes, yet it is invariably accompanied by three key issues: elongated transport paths, reduced transmission rates, and unstable interlayer spacing [29,30]. This kind of membrane however shows superiorities in mechanical stability and scalable production.

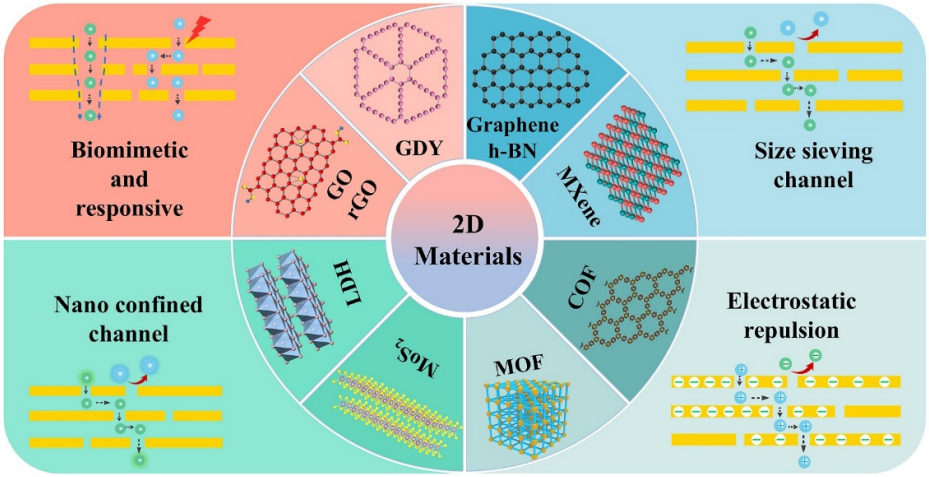

Figure 1. Main two-dimensional materials and types of mass transfer.

Recent innovations in 2D membrane material are flourishing and have shown potential that enables scientists to overcome the trade-off effect in membrane technology [31,32]. It is essential to showcase these advances and discuss some prospectives with researchers. In this review, recent progress in the preparations of high-quality ion-selective membrane based on the 2D materials are first highlighted. It includes the regulation strategies in

ion selectivity and permeability via the physical and chemical approaches. Then, typical promising applications of these membranes in the ion-selective devices are discussed, including seawater desalination [33], ion-selective separation [34], and energy storage and conversion [35–37]. Finally, some valuable insights into future research prospects, challenges, and suggestions to realize the application of 2D materials for high-efficient ion selectivity transport are provided.

2. Materials and Preparation Methods

While the structure of a 2D material governs its properties and potential performance, the synthesis strategy governs its scalability and final application. In recent years, significant breakthroughs have been made in the controllable preparation of 2D membranes based on the bottom-up and top-down methodologies. The strategies of ordered assembly of nanosheets and multi-process exfoliation provide feasible solutions for the efficient and large-scale preparation of 2D membranes. This section typically introduces the prevailing preparation techniques of 2D membranes. For realizing high-flux and high selectivity, it will discuss structural and interfacial regulation and innovation, guided by diverse ion-selective transport mechanisms. Specifically, the preparation of four different 2D materials was introduced, including chemical vapor deposition [38], two-phase interfacial synthesis [39], solution synthesis [40] and exfoliation (Figures 2–5) [41]. The focus is on analyzing the structural characteristics of membrane obtained by various methods and their impact on mass transfer and screening performance.

2.1. Chemical Vapor Deposition

Chemical vapor deposition (CVD), the mainstream technology for preparing 2D materials (graphene, boron nitride, MoS_2, etc.) with few-layer thickness, relies on the precise control of "mass transfer-reaction-formation" process. Key control measures include regulating precursor delivery, optimizing the reaction environment, and performing defect repair [42,43]. By precisely controlling deposition behavior, intrinsic defects can be suppressed and material integrity can be improved, thereby enhancing the material's performance properties.

Precursor design critically determines the intrinsic properties of 2D materials. Self-condensation-assisted CVD leverages temperature gradients to induce temporary benzimidazole precursor droplets on substrates, coordinating with gas-phase iron borane to yield single-layer $Fe_n(bim)_{2n}$ MOFs with atomic thickness and controlled grain sizes (~62 μm) (Figure 2a) [39]. In addition, solid–gas conversion synergistic CVD based on copper oxide precursor layer allows for the direct synthesis of high-quality and well-oriented Cu-BHT MOF membranes. The results indicate that Cu-BHT thin membranes prepared by CVD exhibit large-area uniformity, flatness, high crystallinity, and enhanced carrier mobility [44]. Introducing the deprotonation effect and coordination competition effect of NH_3 can further enhance the performance of Cu-BHT. When the grain area increases from 10 to 10^4 nm^2, the carrier mobility increases from 12 to 31 cm^2 V^{-1} s^{-1}, and the conductivity rises from 0.002 to 3 S cm^{-1} [45] (Figure 2c). Ultrathin self-supporting carbon nitride membranes (UFSCNM) can be prepared by vapor deposition polymerization of melamine and palladium carbonate mixed precursors. Its unique layered structure retains unreacted amino and imino groups, which can dynamically adjust surface charge density through protonation/deprotonation processes (Figure 2b) [46].

Modulating growth mechanism enables precise structural and dimensional control of 2D materials. In the CVD process, the growth kinetics can be systematically adjusted through the precursor concentration and reaction temperature, combined with non-covalent modifications. These adjustments have been successfully applied to alter graphene's growth

process. This facilitates graphene production with tailored pore structures and high surface density, enabling highly selective target separation [47]. Furthermore, a synergistic two-step sputtering/LPCVD (low-pressure chemical vapor deposition) process achieves the precise thickness control of MoS_2 membrane (0.8–8.7 nm) through tuning the sputtering time and flow rates of reaction gas (Figure 2d). This method can also address the problem of large-scale preparation of MoS_2. The resulting membranes exhibit ultrahigh ion conductivity (>1 S cm^{-1}), attributed to highly ordered 2H-phase MoS_2 ion channels that reduce ion migration activation energy [48]. In addition, CVD technology can also be expanded to advanced defect engineering. The size screening mechanism needs the controllable formation of defective graphene. Combined with ultraviolet ozone induction, it can efficiently form selective pores with a diameter of 0.9 nm and fast mass transport pores with a diameter of 3 nm, respectively. The problem of hydrogen proton cross conduction has been effectively solved via such regulating strategy. Devices with ozonated graphene exhibited a 27% enhancement in hydrogen/proton selectivity, a 24% decrease in hydrogen permeation and minimal effect on current output [49].

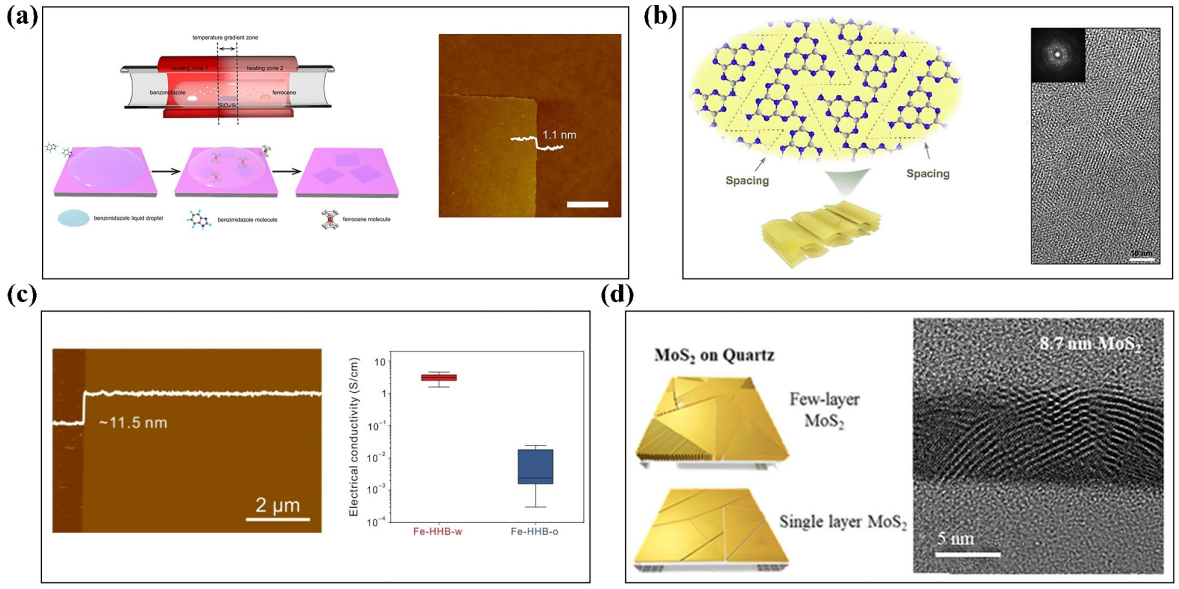

Figure 2. Chemical vapor deposition prepares 2D materials. (**a**) Growth of $Fe_n(bim)_{2n}$ single crystals and its atomic force microscope (AFM) images [39]. (**b**) The structure and high-resolution transmission electron microscopy (HRTEM) and electron diffraction patterns of UFSCNM membrane [46]. (**c**) AFM images and electrical conductivity of Fe-HHB-w thin membranes [45]. (**d**) Diagram of patterned MoS_2 nanomembrane and HRTEM images of MoS_2 nanomembrane with 8.7 nm thickness [48]. Reproduced with permission from (**b**) ref. [46] Copyright (2018), John Wiley and Sons; (**d**) ref. [48] Copyright (2021), American Chemical Society.

2.2. Interface Synthesis

Interface synthesis has emerged as an efficient strategy for preparing large-area, high crystallinity, and low defect 2D materials by precisely controlling molecular orientation and assembly in a confined environment. This method utilizes the interfacial confinement effect (liquid–liquid, gas–solid, liquid–solid, etc.) to guide the ordered arrangement and reaction of molecules or monomers. Thereby, it can construct 2D materials with regular structures. The advantages of interface synthesis are particularly evident in the fabrication of materials such as graphdiyne (GDY) and 2D polymers.

Two-dimensional GDY is an emerging carbon allotrope with intrinsic pores, which was first developed by Prof. Yuliang Li and showcases attractive properties [50]. GDY is prepared based on a typical organic reaction of oxidation cross-coupling reaction, which

is catalyzed by the Cu-based catalysts in the presence of the N-containing organic base. Liquid–solid interface synthesis can precisely regulate the molecular assembly and growth morphologies of GDY, and the GDY nanowalls, nanoporous membrane, (Figure 3a) and flower-like architectures could be controllably synthesized directly [51–53]. When such coupling reaction is carried out in the liquid/liquid interface of water and dichloromethane at room temperature, it could prepare multilayer GDY thin membranes with a thickness below approximately 3.0 nm [54]. According to the structural engineering of monomers, many attractive GDY derivatives have been successfully prepared and have been used in many promising energy-related fields, such as the electrochemical catalyst, energy storage, separation, and so on [55]. In addition, Chi et al. [56] prepared GDY nanosheets on Au (111) surface by thermally induced dehydrogenation coupling reaction using hexa(4-ethylphenyl) benzene as precursor. It has a precise pore size of 5 Å, high pore density, and a single-layer structure with a bandgap of 2.8 eV, exhibiting six-fold symmetry and high thermal stability. This high pore density and angstrom-level precision pore structure provides an ideal channel for efficient ion screening and directional transport. This intrinsic pore density with well-defined pore size of GDY may break the physical and chemical limitations in drilling pores on 2D materials for mass transportation. The pioneer applications in ion-selective transport are discussed below.

Interface synthesis is also applicable to the preparation of 2D polymers, crystalized COF and MOF [57]. Regulating the pre-organized state of monomers at the interface can achieve high crystallinity and ordered layered structures. Feng et al. [58] introduced surfactants into the air–water interface system. As shown in Figure 3b, a few-layer 2D polyimide (PI) was prepared by promoting the ordered arrangement of monomers at the interface and then combining polymerization reaction with surfactants. Meanwhile, ionic covalent organic nanosheets with opposite charges (TpEBra and TpPa-SO_3Na) were also prepared through the gas–water interface synthesis. Due to the strong electrostatic interactions between zwitterionic nanosheets, a staggered stacking structure is formed with strong interlayer interaction, optimizing the pore size distribution of the membrane. The obtained separation membrane was only 41 nm in thickness for testing. The membrane's selectivity is three to six times higher than that of single-phase iCON (TpEBra or TpPa-SO_3Na) membranes [59]. The oil–oil–water three phase interface system provides an innovative approach for controlling the crystallization of 2D polymers. Khashab et al. [60] utilized an intermediate oil layer to precisely regulate the diffusion of triaminoguanidine chloride (TGCl) and 2,5-dimethoxybenzaldehyde (DMTP) precursors, promoting the long-range ordering. TGCl-DMTP COF nanosheets have positively charged guanidine cations (-NH_2^+) in the ordered nanochannels. Powder X-ray diffraction (PXRD) and nitrogen adsorption tests confirmed its crystalline layered structure and uniform pore size distribution of 6.6 Å. These characteristics endow TGCl-DMTP COF nanosheets with a continuous and regular proton transport pathway. The membrane assembled from the nanosheets exhibits excellent ion permeability and selectivity (Figure 3c).

Beyond liquid-phase interfaces, gas–solid interfaces offer enhanced stability and serve as efficient templates for synthesizing ultrathin and highly crystalline 2D materials. For example, trifluorobenzene (TFP) was selected as the solid phase monomer and polydopamine (PDA) was chosen as the gas-phase monomer. These two monomers can rapidly form highly crystalline 2D COF membranes with a thickness of 120 nm on Si/SiO_2 substrate. Due to its ultrathin thickness and ordered pores, the membrane exhibits ultrahigh water permeability and salt rejection rate (Figure 3d) [61]. Furthermore, interface synthesis enables material property customization through functional group engineering. For instance, Wen et al. [62] site-specifically incorporated crown ether moieties via interfacial polymerization, establishing a continuous through-plane hydrogen-bonding network. This ordered net-

work facilitates efficient proton transport while the tightened crown ether cavities sterically exclude Li^+ ions, achieving ultrahigh H^+/Li^+ selectivity (Figure 3e).

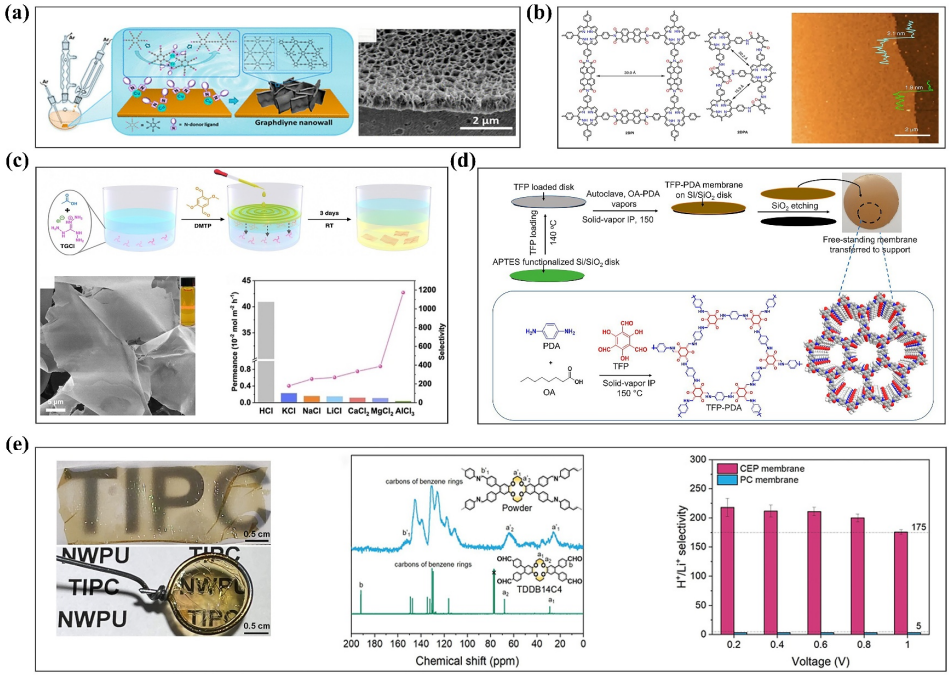

Figure 3. Preparation of 2D materials by interface synthesis. (**a**) GDY synthesis and scanning electron microscopy (SEM) of GDY nanowalls [51]. (**b**) 2D polyamide crystal structure and its AFM image [58]. (**c**) TGCl-DMTP nanosheet preparation. SEM image of TGCl-DMTP nanosheets and its image of Dingdal effect. Permeation of different cations on TGCl-DMTP/PES membranes and selectivity of protons and other metal ions by diffusion dialysis at 0.1M [60]. (**d**) The solid–gas interface synthesis scheme of TFP-PDA membrane and the molecular reaction of TFP-PDA membrane [61]. (**e**) Optical images of CEP on PET (top) and a typical freestanding CEP membrane on a metal ring (bottom). Solid-state ^{13}C NMR spectra of the CEP powder and TDDB14C4 and the selectivity of H^+/Li^+ at different voltages in 0.1 M HCl and 0.1 M LiCl solution [62]. Reproduced with permission from (**a**) ref. [51] Copyright (2015), American Chemical Society; (**b**) ref. [58] Copyright (2019), Springer Nature; (**c**) ref. [60] Copyright (2024), John Wiley and Sons; (**d**) ref. [61] Copyright (2020), American Chemical Society; (**e**) ref. [62] Copyright (2023), John Wiley and Sons.

2.3. Solution Synthesis

Unlike template-dependent methods of both CVD and interfacial synthesis, homogeneous solution synthesis constructs covalent 2D materials through bulk-phase reactions. This approach requires no pre-engineered surfaces or phase interfaces, allowing molecules to freely collide and react in solution. The resulting molecular design flexibility enables both large-scale production and tailored functionalization of 2D materials. Solution synthesis is primarily employed for preparing COFs and MOFs, leveraging rigid structural units to guide directional 2D growth. This process involves (1) ordered arrangement of rigid molecular units via π-π stacking or electrostatic interactions into monolayer structures, followed by (2) planar stabilization through covalent crosslinking or interlayer stacking suppression via electrostatic repulsion [40,63]. For instance, activating methyl carbon atoms in 2,4,6-trimethyl-1,3,5-triazine enables covalent bonding with aldehyde monomers through Knoevenagel condensation. This constructs a 2D COF with triazine units bridged by sp^2-hybridized carbon, which self-assembles into highly crystalline honeycomb structures via π-π stacking. The resulting microscale-thickness COF membranes exhibit high specific surface area (1170 $m^2\ g^{-1}$) and uniform 1.5 nm nanopores. These size-matched channels enable ion-selective transport (Figure 4a) [64].

Collaborative solution-phase strategies optimize structural integrity in 2D materials. At ambient temperature in green solvents, COF condensation reactions are synergized with dopamine (DA) self-polymerization in the study. Shao et al. [65] utilized Schiff-base linkages to covalently bridge COF nanocrystals, effectively "welding" interlayer to eliminate defects and yield ultrathin (125 nm), stable COF membranes (Figure 4b). Increasing DA concentration efficiently accelerates COF nucleation, depositing more poly(dopamine) chains that increase membrane thickness, reduce surface pore size, and enhance nanocrystal interlayer interactions; therefore, collectively improving structural stability.

Solution synthesis further enables transport property regulation through electron-withdrawing group functionalization. Introducing -SO_3H groups creates proton transport sites via hydrogen bonding and Grotthuss mechanisms, forming continuous hydrophilic proton conduction networks. For instance, synthesizing ionic COF (iCOF) membranes from 1,3,5-triformylphloroglucinol (Tp) and 2,5-diaminobenzenesulfonic acid (Pa-SO_3H) yields complete ion channels achieving 75 mS cm^{-1} proton conductivity (Figure 4c) [66]. Spacer engineering enhances performance further. Jiang et al. constructed iCOF nanosheets with terminal -SO_3H groups and variable-length alkyl spacers. The spacer/-SO_3H synergy in medium-length variants enables exceptionally high proton conductivity (889 mS cm^{-1} at 90 °C) through long-range ordered ion channels [67]. For lithium ion conduction, A-B stacked iCOF nanosheets leverage anion/oxygroup "binding-release-hopping" mechanisms to achieve 1.7 mS cm^{-1} Li^+ conductivity at 25 °C (Figure 4d) [68]. The advantages of solution synthesis in preparing COF materials are also applicable to the construction of MOF materials. The coordination interaction between Fe^{3+} and phytic acid can form a metal–organic phosphate membrane (MOPM) under mild conditions. By adjusting the concentration of Fe^{3+}, the pore size of the membrane can be precisely controlled within the range of 0.72–1.82 nm to achieve efficient retention of the target substance. The ultrathin membrane thickness of sub-10 nm significantly shortens the mass transfer path, thereby improving water permeability [69]. This also provides diversified ideas for the synthesis of other 2D framework materials. Although homogeneous solution synthesis simplifies reactions and enables scalable production of 2D materials, significant challenges remain in achieving atomic-level thickness and preventing spontaneous stacking. It still needs additional exfoliation steps for further applications of the formed materials.

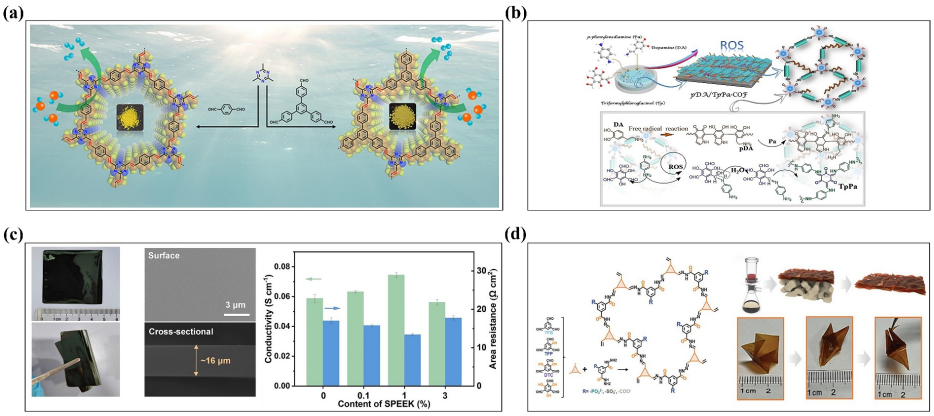

Figure 4. Preparation of 2D materials by solution synthesis. (**a**) Molecular structure of g-$C_{18}N_3$-COF and g-$C_{33}N_3$-COF [64]. (**b**) The process of in situ molecular soldering engineering to fabricate COF membranes [65]. (**c**) Digital photos of TpPa-SO_3H/SPEEK-1% membrane. Surface area and pore volume data of TpPa-SO_3H/SPEEK-x% powders [66]. (**d**) Scheme for the synthesis of iCOF nanosheets [68]. Reproduced with permission from (**a**) ref. [64] Copyright (2019), American Chemical Society; (**b**) ref. [66] Copyright (2023), John Wiley and Sons; (**d**) ref. [68] Copyright (2024), John Wiley and Sons.

2.4. Exfoliation

Unlike direct precursor conversion in the above-mentioned methods, exfoliation employs a top-down fabrication route for the 2D materials with atomic-level thickness. The bulk material is first synthesized, and then it is isolated into 2D architectures via physical/chemical methods. This approach overcomes interlayer van der Waals forces to yield single or few-layer structures. Established techniques include mechanical exfoliation [70], liquid-phase exfoliation [71], ion doping-assisted exfoliation [72], ion exchange [73], and selective etching-assisted exfoliation [74]. Initially developed for graphene, exfoliation now enables scalable production of diverse 2D materials including graphene oxide (GO) [75–77], hexagonal boron nitride (h-BN) [78], transition metal dichalcogenides (e.g., MoS_2) [79], and MXenes [80].

Recent advances in exfoliation technology focus on optimizing efficiency, thickness control, and atomic contamination reduction. Gold-assisted exfoliation leverages strong interfacial bonding for efficient single-step delamination [81]. Layer-controlled exfoliation deposits metal films (Au, Pt, Ni, Co) onto graphene surfaces, utilizing interfacial energy differentials between metal–graphene and graphene–graphene layers to precisely regulate thickness (Figure 5a) [82]. Liquid-phase exfoliation using liquid gallium achieves high-aspect-ratio nanosheets under mild conditions through intercalation and shear forces (Figure 5b) [83]. However, exfoliation-induced defects, surface imperfections, and interlayer misalignment remain challenging. These microstructural irregularities hinder precise dimension control of interlayer channels, directly compromising molecular/ion transport efficiency [84]. Therefore, in order to achieve high-throughput transmission and precise separation, it is usually necessary to combine the "exfoliation and post adjustment" strategy for fine optimization.

Intercalation-assisted exfoliation represents a critical pathway for fabricating 2D nanosheets. Strategically inserting spacer molecules between graphene oxide (GO) layers enables precise interlayer spacing control, achieving size-selective ion/molecular sieving [85]. Sequential exfoliation and K^+ intercalation can precisely regulate GO interlayer spacing to 1 Å resolution (Figure 5c) [86]. Beyond precise dimensional control, scalable defect-free production is essential—shear rate optimization enables large-scale graphene exfoliation [87], while plasma jet technology facilitates ultra-rapid (<1 kg/h) graphene production [88]. Hexagonal boron nitride (h-BN) leverages its graphene analogous-layered structure, where high surface charge density generates strong electrostatic interactions within sub-nanometer channels, enabling efficient ion-selective membranes (Figure 5d) [89]. Li^+-assisted hydrothermal exfoliation yields h-BN nanosheets with 10 μm lateral dimensions and tunable 1–3 nm thickness (Figure 5e) [90]. For phase-variable MoS_2 (1T/1T′/1T″), phase transition-induced structural instability causes interlayer defects that compromise permeability. Combining Li^+ intercalation with vacuum filtration stabilizes high-quality 1T′ phase laminates, ensuring efficient water transport [91]. Building on this, Voiry et al. [92] developed an integrated strategy where Li^+ exfoliation and covalent functionalization synergistically tune MoS_2 interlayer spacing and surface chemistry, significantly enhancing $Na^+/Li^+/K^+$ selectivity.

Choi et al. [93] obtained a 2D carbon material (o-2DZTC) with vertically ordered micropores and high pore density by ultrasonic exfoliation using large-sized IWV zeolite as a template (Figure 5f). The aligned micropores and uniform pore distribution minimize transport pathways, enabling exceptional water permeability and salt rejection. Ion exchange exfoliation further expands methodological diversity: MXene membranes assembled through poly(ionic liquid)-assisted exfoliation leverage electrostatic interactions to tune nanochannel surface chemistry. The anion exchange capacity of PILs establishes hydrophilic/hydrophobic nanochannels that simultaneously enhance water flux and ion

rejection [94]. In addition, the combination of molten salt etching and tetrabutylammonium hydroxide (TBAOH) intercalation exfoliation process was used to prepare self-supporting MS-$Ti_3C_2T_x$ MXene nanosheets. Limiting TBAOH exposure mitigates surface hydroxyl oxidation and prevents dense restacking, significantly improving ion transport efficiency [95]. Similarly in vermiculite membranes, alkyl chain length modulation of crosslinkers precisely regulates interlayer spacing and charge distribution. This dual-control strategy optimizes ion transport while dramatically enhancing chemical stability (Figure 5g) [96].

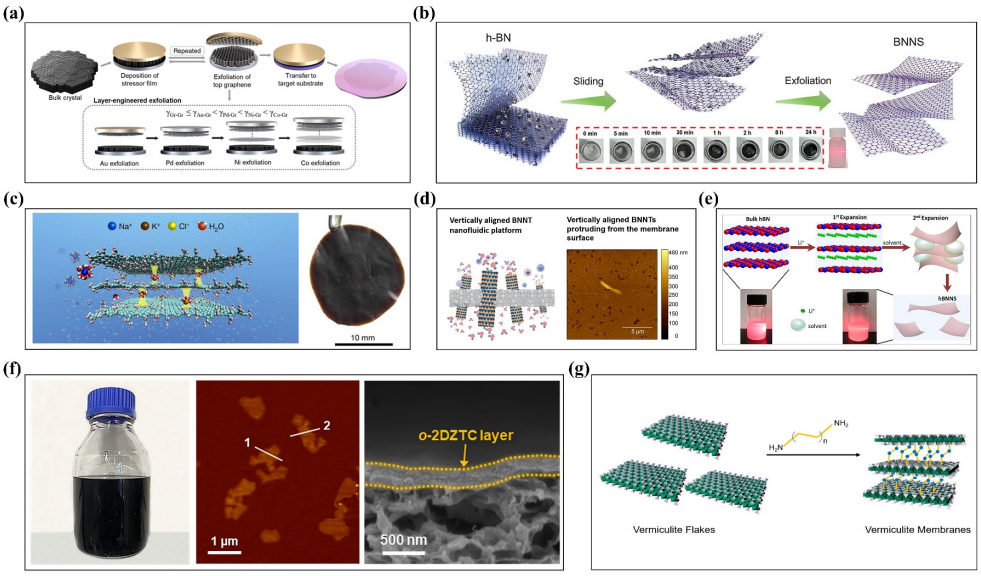

Figure 5. Preparation of 2D materials through exfoliation. (**a**) Large-scale exfoliation of graphene in layered engineering. The inset shows the change in the number of graphene layers according to the relative binding energy between graphite and a metal membrane [82]. (**b**) h-BN exfoliation process of liquid metal [83]. (**c**) Ion retention achieved by K^+ fixed GO membrane spacing. Photo of freestanding oxidized graphene suspension (GOM) [86]. (**d**) The fabrication process of an alkanediamine crosslinked VM [89]. (**e**) The hydrothermal peeling process of Hbnns [90]. (**f**) Photograph of N-methylpyrrolidone solution containing exfoliated 2DZTC (o-2DZTC). AFM image of o-2DZTC particles on silicon wafer. Surface SEM image of o-2DZTC membrane [93]. (**g**) Ion transport mechanism through BNNT nanofluid platform. AFM image of vertically arranged BNNTs protruding from the surface of polymer matrix [96]. Reproduced with permission from (**b**) ref. [83] Copyright (2014), John Wiley and Sons; (**c**) ref. [86] Copyright (2017), Springer Nature; (**d**) ref. [89] Copyright (2019), Elsevier; (**e**) ref. [90] Copyright (2022), Elsevier; (**g**) ref. [96] Copyright (2022), American Chemical Society.

3. Application of 2D Materials

The development of thinner, stronger membranes for ion-selective transport represents a key advancement path in membrane technology, driven by the need to overcome fundamental trade-off effects in transport phenomena. Two-dimensional materials intrinsically have stronger mechanical performance for preparing tougher and thinner membrane than common polymers. Owing to their atomic-scale thickness, tunable sub-nanometer to nanometer-sized channels, and rich surface chemistry, 2D materials hold revolutionary potential for playing the crucial role in the ion-selective transport-related applications [97]. Many significant progresses achieved recently have showcased the ion-selective transport of 2D materials with diverse porous sizes and functions. In this section, some typical ion-selective transport-related applications of 2D membranes are introduced, such as seawater desalination, high-value ion separation, osmotic energy conversion, and fuel cells (Figure 6), as well as their advantages in saving energy, prompting the efficiency and

lifespan (Table 1). Meanwhile, strategies to overcome the trade-off effect in these domains are further proposed.

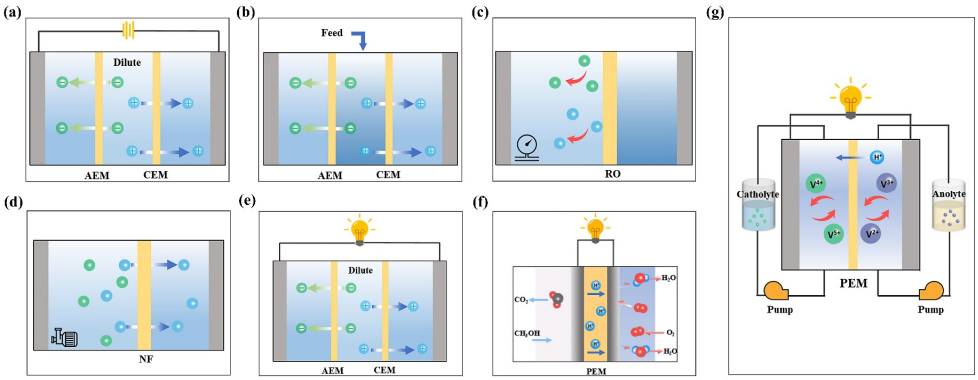

Figure 6. The application of 2D materials. (**a**) Electrodialysis. (**b**) Diffusion dialysis. (**c**) Reverse osmosis. (**d**) Nanofiltration. (**e**) Reverse electrodialysis. (**f**) Direct methanol fuel cell. (**g**) Vanadium redox flow battery.

3.1. Desalination Seawater

As global water resources become increasingly scarce, particularly with the growing prominence of freshwater shortages, seawater desalination technology is gaining widespread international attention as an effective solution for water resource development. The advancement of energy-efficient desalination technologies has emerged as a key research priority. Two-dimensional ion-selective membranes have emerged as pivotal technologies for enhancing seawater desalination efficiency due to their unique interlayer architectures and nanopore characteristics [98]. These atomically thin membranes exhibit exceptional ion selectivity, where their ultrathin structure drastically shortens ion transport pathways and reduces resistance.

Graphene, the earliest engineered 2D material, has demonstrated significant potential in desalination [99]. Nanoporous graphene membranes (NGMs) feature atomic-layer thickness and form 2D nanochannels through in-plane nanopores, creating ordered pathways that facilitate rapid water transport [100]. Similarly, controlled deposition techniques induce ordered alignment in single-layer graphene oxide (SLGO) nanosheets, yielding regular sub-nanometer interlayer channels that promote fast water permeation while effectively blocking salt ions through size exclusion [101]. Further advances include quasi-vertical asymmetric channels in graphene oxide membranes, which shorten transport pathways while increasing channel density. This architecture achieves ultrahigh water permeability (2647 L m^{-2} h^{-1} bar^{-1}) and exceptional NaCl rejection (99.9%) (Figure 7a) [102]. Composite membranes incorporating porous graphene (PG) into GO matrices enable solvent-responsive channel size modulation, allowing intelligent switching between water and solvent screening modes [103]. However, transmembrane co-transport of anions and cations reduces salt rejection efficiency. To address this, charge-regulated nanochannels are essential for ion-selective separation. Quan et al. [104] employed electrostatic induction assembly to embed sodium polystyrene sulfonate (PSSNa) into amine-crosslinked reduced GO (rGO), creating ArGO-PSSNa membranes. Fixed charges on pore walls drive cation/anion rearrangement, forming overlapping electrical double layers (EDLs) that deplete co-ions while enriching counterions, overcoming co-transport limitations. Alternatively, inserting alumina pillars between vermiculite layers enhances interlayer interactions and water permeability. Pre-pillaring Na^+ doping reversibly modulates membrane surface charge, significantly improving monovalent/multivalent salt separation efficiency through electrostatic effects [105].

The exceptional desalination performance of graphdiyne (GDY) membranes stems from precise control of intrinsic sub-nanometer pores, where size-sieving effects enable both high water flux and salt rejection. GDY membranes fabricated on porous copper hollow fibers (PCHF) exhibit nanoporous structures that leverage intrinsic pore sieving to achieve rapid water permeability (742 ± 32 L m^{-2} h^{-1}) and >99.9% NaCl rejection from 3.5 wt% NaCl solutions (Figure 7b) [106]. In GDY membranes featuring 1D nanochannels, selective transport of water molecules and H^+ occurs via 'single-file arrangement friction' and Grotthuss proton-hopping mechanisms. These achieve water permeability of 593 L m^{-2} h^{-1} bar^{-1}, 99.7% salt rejection, and unprecedented water/Na^+ selectivity (5.96×10^4), thereby overcoming the flux–selectivity trade-off (Figure 7c) [107]. This ordered nanochannel design extends to conjugated polymer framework (CPF) membranes. Ultrathin (1 nm) CPF membranes contain rhombic sub-nanometer channels (10.3 × 3.7 Å), enabling precise molecular sieving with water flux of 202 L m^{-2} h^{-1} bar^{-1}, >99.5% salt rejection, and water/NaCl selectivity of 6900 [108].

Beyond single-dimensional materials, mixed-dimensional architectures enhance performance. Wu et al. [109] engineered 2D nano-polyamide membranes with embedded 1D nanotubes (NoN) via interfacial polymerization, achieving 30.0 L m^{-2} h^{-1} bar^{-1} water permeability and 99.0% Mg_2SO_4 rejection (Figure 7d). Similarly, mixing 2D COF nanosheets with 1D cellulose nanofibers (CNFs) strengthened interlayer interactions, reducing defects while enabling precise molecular sieving through controlled nanopore shielding [110]. Long-term stability remains critical for practical deployment. Al^{3+} intercalation in MXene membranes forms stable crosslinks with surface oxygen groups (-O/-OH), suppressing swelling and enhancing chemical stability. This yielded 99.5–99.6% NaCl rejection from 0.1 M NaCl solutions (Figure 7e) and maintained performance over 400 h (Figure 7f), demonstrating highly efficient and durable desalination [111].

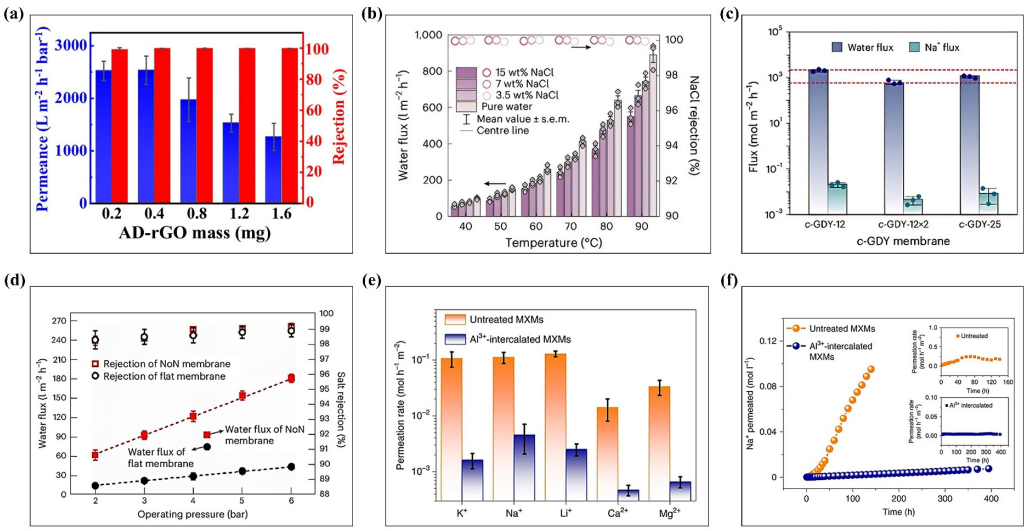

Figure 7. Water permeability and salt rejection rate of 2D membrane materials. (**a**) The permeability and $CuSO_4$ rejection of AD-rGO membranes of different qualities at 50 °C [102]. (**b**) Flux and NaCl rejection rate of GDY@PCHF membrane with different temperature [106]. (**c**) Water and reverse Na^+ flux of c-GDY-12, c-GDY-12×2, and c-GDY-25 membranes [107]. (**d**) Nanofiltration performance of mixed dimension polyamide membrane and flat membrane under different operating pressures [109]. (**e**) The permeation rates of untreated MXM and Al^{3+} embedded MXM for different ions [111]. (**f**) The long-term permeation rate of Na^+ by untreated MXM and Al^{3+} embedded MXM [111]. Reproduced with permission from (**b**) ref. [106] Copyright (2023), Springer Nature; (**c**) ref. [107] Copyright (2025), Springer Nature; (**d**) ref. [109] Copyright (2024), Springer Nature; (**e**) ref. [111] Copyright (2020), Springer Nature.

3.2. High-Value Ion Separation

Ionic separation technology plays a pivotal role in extracting high-value metals in wastewater and battery material recovery [112]. Achieving high selectivity primarily relies on techniques like electrodialysis [113] and diffusion dialysis [114], where membrane design constitutes the core innovation. Current strategies extend beyond traditional approaches (pore size control, charge optimization, and confined transport) to include biomimetic ion channel design, an innovative pathway overcoming separation trade-offs by mimicking biological mechanisms for efficient, controllable ion transport. In this part, the recovery of Li by the 2D membrane is discussed as the representative.

For precise nanopore control, an electrochemical repair strategy was employed to mask non-selective macropores in graphene. Using piperazine (PIP) and polyethyleneimine (PEI) as anchoring molecules, pores >0.7 nm were selectively plugged, yielding membranes with exceptional ion selectivity: K^+/Na^+ = 20, K^+/Mg^{2+} = 330, and Li^+/divalent ions >900 (Figure 8a) [115]. Complementing size exclusion, introducing strong electrostatic repulsion further enhances selectivity. Charged monomer (C_2VI) copolymerization with crosslinker (C_4VI_2) created ultrahigh-charge-density ion exchange membranes. Charge repulsion boosted ion conductivity by 4.5–13 times while maintaining selectivity, thereby breaking the flux–selectivity trade-off (Figure 8b) [116]. Nanochannel confinement ensures long-term stability of pore/charge environments. Wang et al. [117] crosslinked multivalent cations with sodium alginate (SA) to form stable hydrogel pillars between $Ti_3C_2T_x$ layers, fixing interlayer spacing at 7.4 $\pm$ 0.2 Å. In acid recovery systems, the permeation rate of H^+ by the membrane was about 800 times higher than that of Fe^{2+} (Figure 8c). And in the nanofiltration, the membrane had a rejection rate of 100% for Na_2SO_4. Its comprehensive performance far exceeded traditional membrane materials.

Biomimetic ion channels achieve selective ion separation through structural complementarity and electrostatic interactions. For instance, γ-polyglutamic acid (γ-PGA) functionalized MXene nanosheets create dynamic ion-pairing transport mechanisms [118]. Unlike conventional size exclusion, this design leverages γ-PGA's synergistic binding sites for anions and cations, exploiting energy barrier differences to achieve K^+/Mg^{2+} selectivity >10.3 while enabling tunable permeation rates across two orders of magnitude (Figure 7d). Similarly, imidazole/sulfonic acid-modified GO (i-GO) membranes utilize rigid imidazole structures for physical confinement and sulfonic groups for chemical selectivity, attaining K^+ permeability of 1.36 mol m^{-2} h^{-1} and K^+/Mg^{2+} selectivity of 9.11 [119]. Covalently modified bilayer graphene achieves atomic-scale pore control with exceptional cation selectivity: K^+/Li^+ (48.6), K^+/Cl^- (76), and H^+/Cl^- (59.3) [120]. The membrane's atomic thickness minimizes transport resistance, while covalent functionalization imposes steric/electrostatic barriers to Cl^-/Li^+ transport, enabling efficient K^+/H^+ permeation. Tian et al. [121] developed <001>-oriented Zn-TCPP membranes with sub-nanometer pores optimized for K^+ transport. Divalent cations (Mg^{2+}, Ca^{2+}, Mn^{2+}, Co^{2+}, Ni^{2+}) exhibited variable channel-blocking behavior regulated by $Zn_2(COO)_4$ affinity differences (DFT-verified), enabling dehydration-controlled ion gating via combined size exclusion and M^{n+}-coordination. Mimicking biological Na^+/K^+ switching, pH-responsive COF-Cys membranes were engineered through cysteine-grafted COF-V channels [122]. These exhibited dynamic ion selectivity reversal: K^+/Na^+ = 1.7 (pH 3.8) → Na^+/K^+ = 2.9 (pH 8.9) (Figure 8e). pH-dependent cysteine conformation/charge states differentially regulate Na^+/K^+ permeability, replicating biofilm potential reversal and advancing smart membrane design.

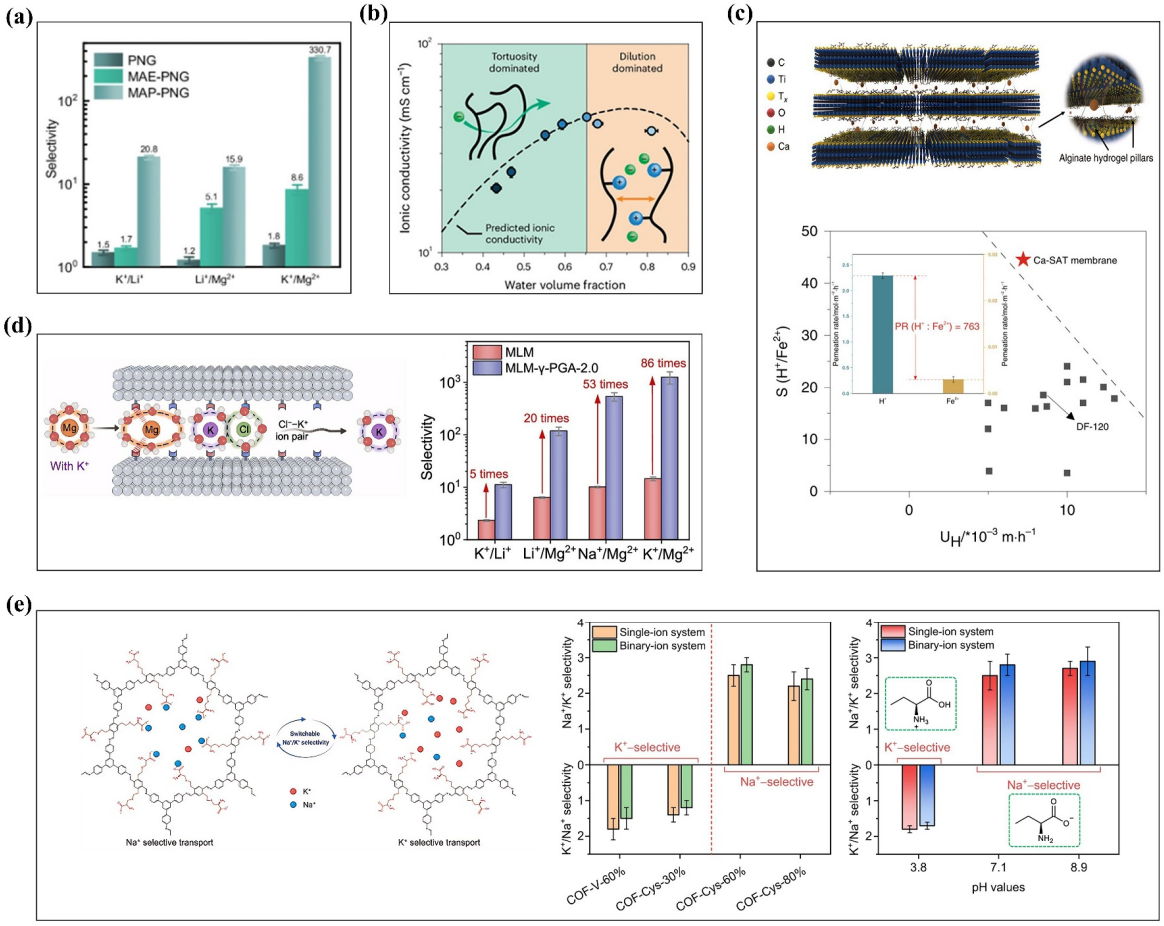

Figure 8. Ionic separation performance of 2D membrane materials. (**a**) Selectivity of PNG, MAP-PNG, and MAE-PNG between K^+, Li^+, and Mg^{2+} [115]. (**b**) The relationship between the water volume fraction and ion conductivity of UHCD membrane after equilibrium in deionized water [116]. (**c**) Crosslinked SA-$Ti_3C_2T_x$ membranes with different multivalent M^{n+} crosslinks (Ca^{2+}, Ba^{2+}, Mn^{2+}, and Al^{3+}). Comparison of separation performance between Ca-SAT membrane and previously reported ion exchange membranes as well as commercial DF-120 membrane [117]. (**d**) The mechanism of K^+ regulating Mg^{2+} permeation through MLM-γ-PGA membrane. Comparison of ion separation performance between MLM-γ-PGA-2.0 and MLM [118]. (**e**) Cysteine functionalized COF membrane achieves switchable Na^+/K^+ selectivity. The selectivity of COF-Cys-x membrane towards Na^+/K^+. Influence of pH on the Na^+/K^+ selectivity of COF-Cys-60% membranes [122]. Reproduced with permission from (**b**) ref. [116] Copyright (2025), Springer Nature; (**d**) ref. [118] Copyright (2025), American Chemical Society.

3.3. Osmotic Energy Conversion

Osmotic energy derived from the salinity gradient between seawater and freshwater represents a promising clean energy source. Reverse electrodialysis (RED), a straightforward technology for harvesting this salinity gradient energy to generate electricity [123], relies on highly ion-selective membranes, including cation exchange membranes (CEMs) and anion exchange membranes (AEMs) [98]. To enhance the performance of 2D materials for osmotic energy harvesting, some effective strategies have been employed to tune the ion-selective transport. In this part, we mainly discuss several impressive strategies including optimizing channel structure, modifying surface charge distribution, constructing heterogeneous structures, and applying external energy fields (e.g., light, heat), which greatly boost ion transport kinetics and optimize the energy harvesting.

Specific assembly methods enable the construction of graphene-based materials into 2D nanofluidic membranes utilizing their inherent pores, achieving both high permeability

and selectivity [124]. For example, mixing graphene oxide (GO) with sodium polyacrylate (PAAS) and coating the mixture onto a polyvinyl alcohol (PVA) substrate yielded a mesoporous structure that significantly enhanced ion permeability and selectivity. Simulated under seawater/river water osmotic energy harvesting conditions, this membrane achieved a maximum power density of 13.8 W m^{-2}, substantially exceeding the industrial standard of 5 W m^{-2} (Figure 9a) [125].

Separately, high-density sub-nanoporous graphene (HGN) membranes fabricated via interface aggregation technology exhibited pore sizes <10 Å and pore densities up to 10^{12} cm^{-2}. By modulating the charge states of NH_2 groups within the nanopores, these HGN membranes delivered power densities exceeding 100 W m^{-2} (Figure 9b) [126]. Beyond pore engineering, regulating the interlayer spacing of 2D materials enables size-selective ion sieving analogous to pore size control. Introducing charged intercalation agents can simultaneously enhance membrane ionic conductivity and selectivity, significantly improving osmotic energy conversion performance [127]. Chen et al. [128] demonstrated this by inserting sodium polystyrene sulfonate (PSS) spacers (bearing -SO_3H groups) into MXene interlayers. This strategy achieved simultaneous interlayer expansion and increased charge density, yielding a power density of 1.57 W m^{-2} under seawater/river water conditions using a minimal test area (0.24 mm^2) (Figure 9c,d). The membrane also exhibited excellent monovalent ion separation capability (Figure 9e).

Furthermore, charged functional groups within 2D material membranes serve as active sites for selective ion interactions, enhancing selectivity [129]. Feng et al. [130] prepared a fully crystalline 70 nm-thick 2D polyimide (2D-PI) membrane via SMAIS technology. Density functional theory (DFT) calculations confirmed that oxygen and imine nitrogen atoms act as active sites, strongly coordinating Na^+ ions. This resulted in a Na^+ selectivity coefficient of 0.98, corresponding to Na^+/Cl^- selectivity of ~84 (Figure 9f). This approach overcomes the traditional conductivity–selectivity trade-off, achieving a high power density of 53 W m^{-2} in osmotic energy conversion (Figure 9g).

Constructing heterogeneous composite structures represents another effective approach for preparing high-performance 2D membrane materials. The nano-heterogeneous channels within such composites significantly reduce membrane resistance and enhance ion transport efficiency. For instance, MXene/BN composite membranes with 2D/2D heterostructures exhibit reduced internal resistance and improved ion transport, yielding twice the power density of pure MXene membranes [131]. Similarly, in heterogeneous MXene/PBONF membranes, the strong interfacial binding between PBONF and MXene endows the 2D nanofluidic membrane with high mechanical strength and excellent ion selectivity. Under concentration gradients of 50 and 500, these membranes achieved power densities of 15.7 W m^{-2} and 65.1 W m^{-2}, respectively, while maintaining long-term stability [132], providing a robust solution for osmotic energy conversion. Embedding ZIF-8 crystals into an MXene matrix constructs nano-to-angstrom scale heterogeneous channels. This architecture synergistically combines ZIF-8's size-sieving capability with MXene's charge effect, achieving a power density of 48.05 W m^{-2} and an ion selectivity of 0.906 (Figure 9h) [133]. Furthermore, the heterostructure enables pH-responsive regulation of MXene's pore size and charge distribution, overcoming the inherent trade-off between permeability and selectivity (Figure 9i) [134]. However, conventional approaches relying on static chemical modifications and fixed salinity gradients face limitations in performance and environmental adaptability, prompting the need for more efficient energy harvesting methods. Emerging light-driven technologies show significant potential: analogous to electron–hole separation in organic photovoltaics, rGO/CMP Janus membranes generate photo-induced transmembrane electric fields that drive efficient ion transport through

porous membranes. This photovoltaic-inspired ion transport concept demonstrates considerable promise for energy conversion (Figure 10a) [135].

Additionally, combining ordered layered ion channels with photothermal guidance mechanisms can synergistically enhance conversion efficiency. Under practical asymmetric illumination, significant transmembrane temperature gradients develop. For example, g-C_3N_4-modified MXene/regenerated cellulose composite nanomembranes achieved 5.9 W m^{-2} power density via photothermally driven ion transport (Figure 10b) [136]. MXene membranes under combined temperature and salinity gradients showed a 133% increase in output power density efficiency (Figure 10c) [137]. Innovatively, Wang et al. [138] developed luminescent Cu-TCPP 2D nanofluidic membranes, where inherent nanopores, interlayer channels, and photothermal effects collectively drive ion transport without requiring a salinity gradient. This system achieved a power density of 31.92 W m^{-2} under pure light illumination (Figure 10d).

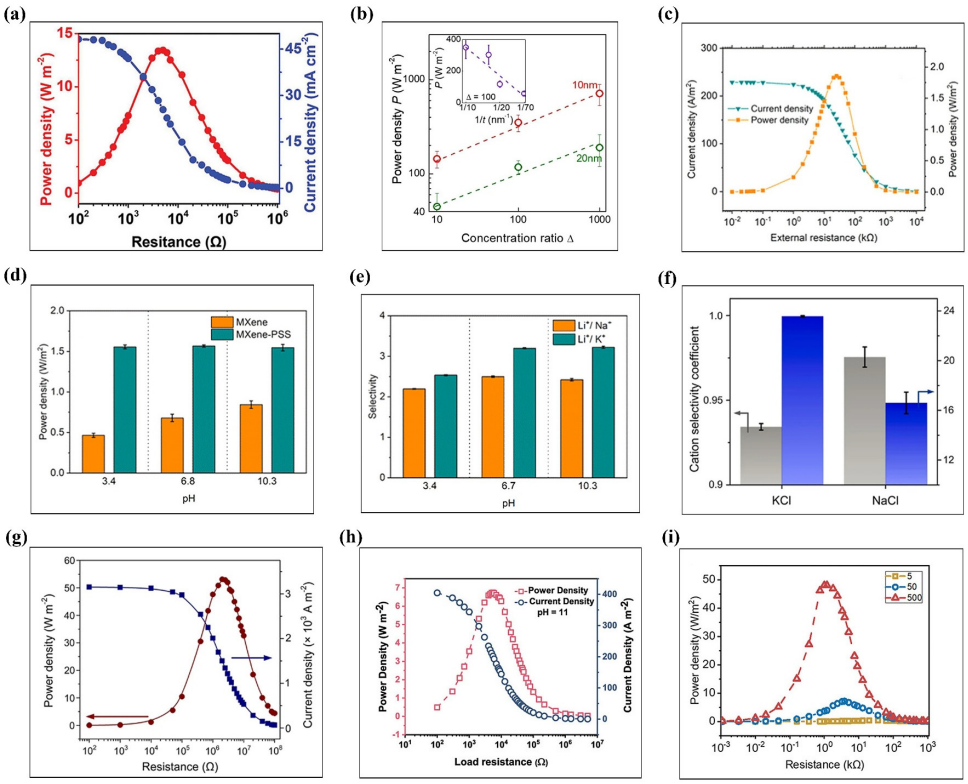

Figure 9. Osmotic energy conversion of 2D membrane materials. (**a**) The current density and power density of GPPS membrane for collecting osmotic energy in real river water and seawater [125]. (**b**) Power density of holey-graphene-like membranes at different concentrations [126]. (**c**) Current density and power density of MXene-PSS membrane in 0.01 and 1 M KCl diluted and concentrated solutions [128]. (**d**) The power density of MXene and MXene-PSS membranes at different pH [128]. (**e**) The metal ion selectivity of MXene and MXene-PSS membranes at different solution pH [128]. (**f**) Ionic selectivity coefficient in NaCl and KCl solutions with a concentration gradient of 10 times [130]. (**g**) The power density of the 2DPI membrane under the mixing of artificial river water and seawater [130]. (**h**) Power density of MXene/ZIF-8 hybrid membrane at different concentration gradients [133]. (**i**) Power density and current density under a 50-fold concentration gradient of the MXene/PS-b-P2VP membrane [134]. Reproduced with permission from (**a**) ref. [125] Copyright (2024), John Wiley and Sons; (**b**) ref. [126] Copyright (2020), American Chemical Society; (**c**) ref. [128] Copyright (2022), American Chemical Society; (**h**) ref. [133] Copyright (2022), John Wiley and Sons; (**i**) ref. [134] Copyright (2021), John Wiley and Sons.

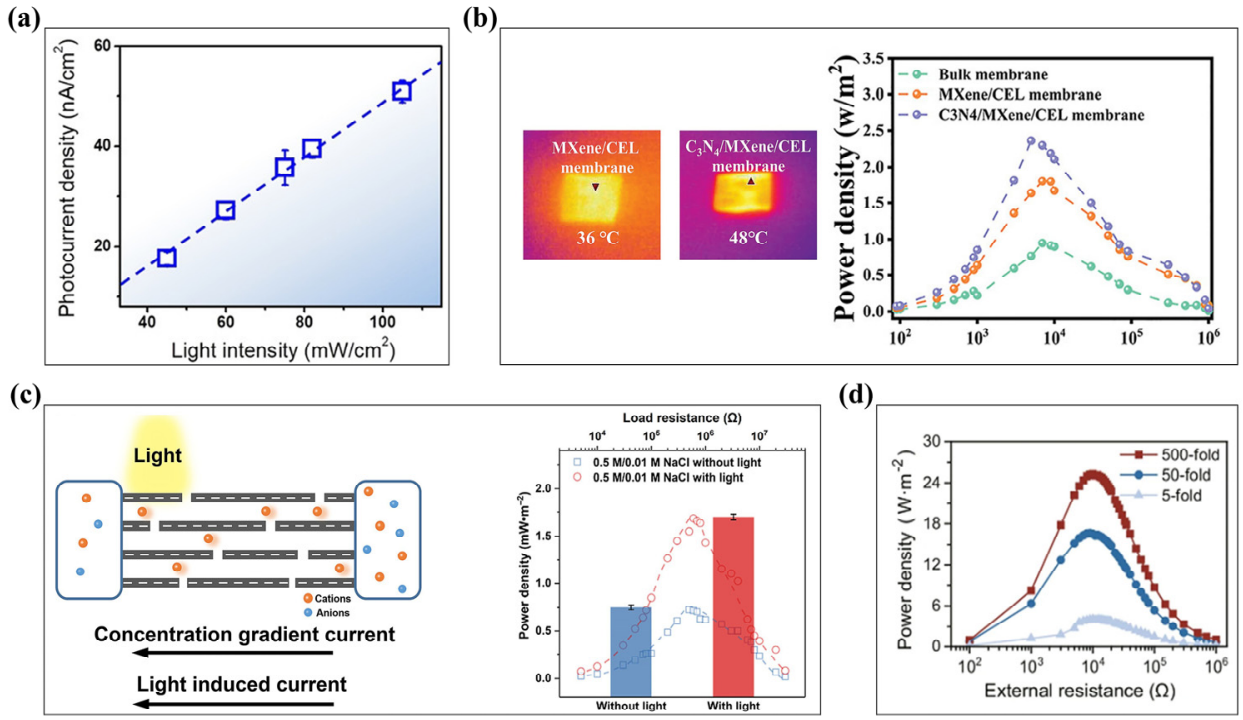

Figure 10. Light and heat responsive 2D materials for energy harvesting. (**a**) The photocurrent density measured under different light intensities [135]. (**b**) Infrared thermography of MXene/CEL and C_3N_4/MXene/CEL membranes after illumination. Comparison of the power density of bulk membrane, MXene/CEL membrane, and C_3N_4/MXene/CEL membrane [136]. (**c**) Ion-driven model in MXene membrane under illumination. Power density of MXene membrane under illumination and non-illumination for a salinity difference of 50 times [137]. (**d**) Power density of Cu-TCPP membrane under different salinity gradients [138]. Reproduced with permission from (**a**) ref. [135] Copyright (2020), John Wiley and Sons; (**b**) ref. [136] Copyright (2025), John Wiley and Sons.

3.4. Proton Conduction in Energy Applications

Proton conduction is a critical process in various electrochemical devices, including fuel cells, flow batteries, and water electrolyzers [139,140]. Polymer proton exchange membranes (PEMs) serve as essential carriers for this function. When developing high-current-density electrochemical devices, reducing PEM thickness, and enhancing proton conductivity become crucial strategies. However, decreasing membrane thickness directly compromises both ion-selective transport and mechanical integrity, significantly impairing device longevity. Consequently, developing ultrathin membranes that simultaneously achieve high proton-selectivity, superior conductivity, and robust mechanical strength presents new fundamental and engineering challenges. Two-dimensional porous materials with proton-transport functionality demonstrate significant potential to overcome this challenge. They enable effective reduction in membrane thickness while simultaneously enhancing ion selectivity and improving mechanical strength, offering promising prospects for advancement.

3.4.1. Proton Conductivity

While defect-free graphene blocks gases/liquids, it has excellent proton permeability [141]. Disordered graphene with high-density eight-atom ring defects not only fully blocks molecules but also shows ~1000 times higher proton permeability than defect-free graphene (Figure 11a) [142]. By introducing nitrogen defects through nitrogen plasma treatment, the rapid protonation/deprotonation cycle of nitrogen sites boosts proton transport. Nitrogen-doped graphene membranes achieve conductivity of 1.4×10^5 S m^{-2} in 1M

HCl (Figure 11b) [143]. Graphene-like 2D TiO_2 also exhibits proton transport properties. The PEMs based on this structure can attain a conductivity of 100–200 S cm^{-1} under high-temperature conditions (Figure 11c) [144]. Additionally, proton-exchanged mica exhibits excellent proton conductivity. The surface conductivity of its 5 Å-wide nanochannels exceeds 100 S cm^{-1} at 500 °C, which is 1–2 orders of magnitude higher than graphene or h-BN [145].

The synthesis of GDY materials has opened new avenues in 2D material development. Monolayer GDY exhibiting no stacking and in-plane intrinsic pores was synthesized via hexaethynylbenzene coupling within the confined space between MXene layers. The freestanding ML-GDY demonstrated a room-temperature conductivity of 5.1×10^3 S m^{-1} and an average carrier mobility of 231.4 cm^2 V^{-1} s^{-1} (Figure 11d) [146]. Subsequent annealing treatments modulated GDY diyne bond density and oxygen-containing group content, further enhancing its mixed proton–electron conductivity (Figure 11e) [147]. A proposed "transparent proton transport" mechanism explains GDY's exceptional proton conduction: an intrinsic transmembrane hydrogen-bonding network provides an ideal proton-conducting pathway, enabling protons to permeate GDY membranes with water-like mobility [148]. Mao et al. [149] oxidized GDY with concentrated nitric acid to produce graphdiyne oxide (GDYO), preserving the carbon skeleton while introducing hydrophilic groups to form a 2D micro-layered structure. GDYO exhibits exceptional water uptake (84 wt% at 100% RH, Figure 11f), attributed not only to surface hydrophilicity but also to its unique sp/sp^2-hybridized carbon skeleton, which exhibits strong water affinity. Crucially, this skeleton promotes hydrogen-bond formation between water molecules, expanding the hydrogen-bonding network. This network significantly increases proton concentration and creates continuous conduction pathways, enabling ultrahigh proton conductivity (0.54 S cm^{-1} at 100% RH and 348 K).

For 2D organic frameworks, prominent materials in proton conduction research, optimization relies on three key strategies: (1) ordered channel design, (2) precise chemical modification, and (3) interface compatibility regulation. Together, these construct low-tortuosity proton pathways and reduce proton-hopping energy barriers [150]. Regulating precursor hydrophilicity enables compact stacking of covalent organic framework (COF) membranes, optimizing the hydration environment within proton transport channels. Introducing proton exchange groups enhances membrane ion exchange capacity (IEC), thereby boosting proton conductivity (Figure 11g) [151]. Furthermore, leveraging interlayer confinement effects in COFs allows precise arrangement of hydrophilic ligands (e.g., -SO_3H groups) to construct localized ultrafast proton transport pathways via short hydrogen bond (SHB) networks. These SHB networks dramatically reduce proton transport barriers, enabling low-energy-barrier proton transitions. COFs incorporating SHB achieve exceptional proton conductivity (1389 mS cm^{-1}) [152]. This confinement strategy extends to other materials; bismuth iodide oxide (BiOI) nanosheets assembled into 2D nanocapillaries increase the number of short hydrogen bonds within confined nanochannels by 12-fold within hydroxide exchange membranes (HEMs). This creates efficient shortcuts for Grotthuss-type anion transport, achieving high ionic conductivity (168 mS cm^{-1} at 90 °C, Figure 11h) [153].

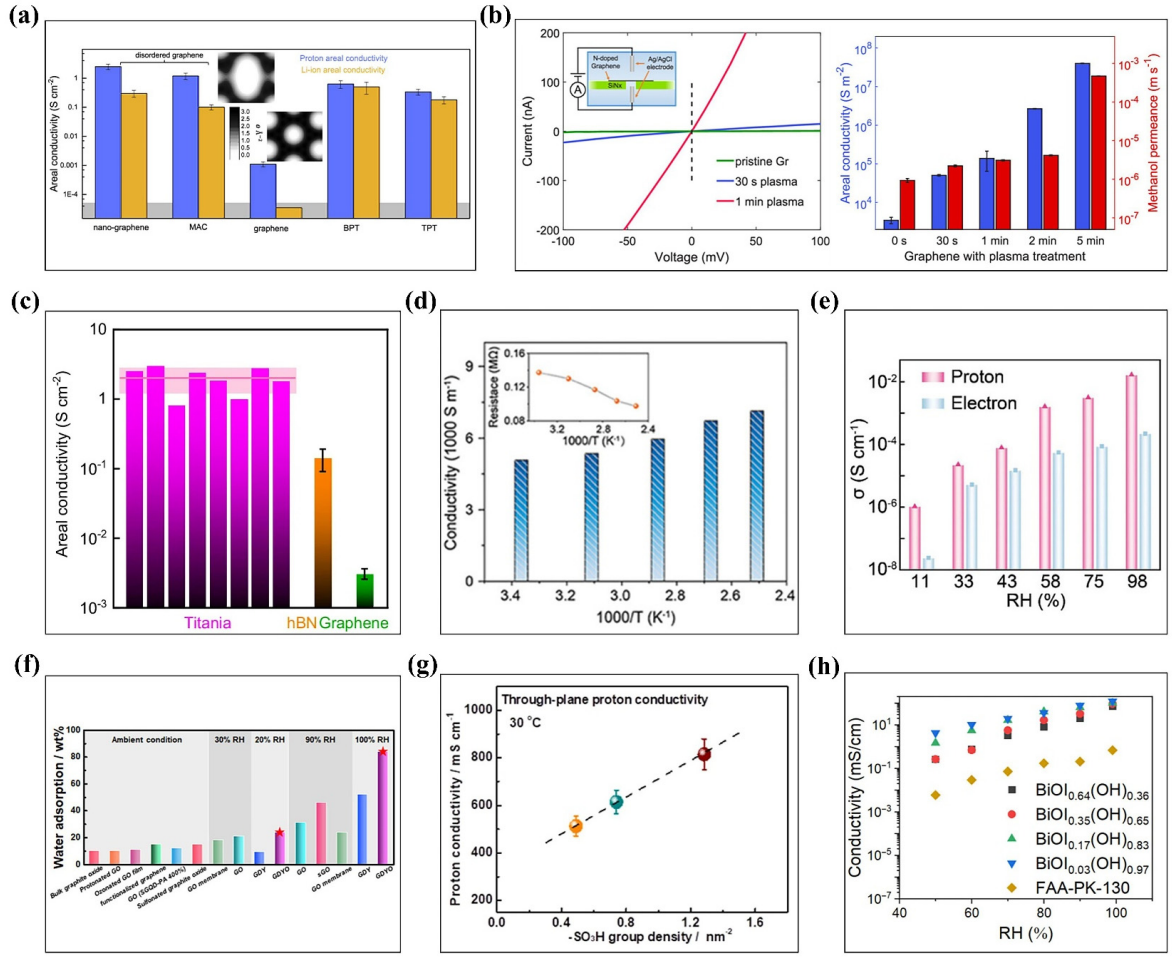

Figure 11. (**a**) Proton conductivity of 2D materials. Statistics for proton and Li-ion areal conductivities measured for different 2D carbon membranes [142]. (**b**) Conductivity measurement device for NGM. The areal proton conductivity and methanol permeance of different membranes [143]. (**c**) Proton surface conductivity of titanium dioxide, graphene, and hBN [144]. (**d**) Conductivities and resistances (inset) of ML-GDY as an inverse function of temperature [146]. (**e**) Proton conductivity and electron conductivity of GDY at different relative humidities [147]. (**f**) Comparison of water absorption properties of GDYO and GO matrix proton conductors [149]. (**g**) The surface proton conductivity of iCOFMs at 30 °C in 1 M HCl solution [151]. (**h**) Ionic conductivity of $BiOI_{1-x}$ $(OH)_x$ under different humidity conditions [153]. Reproduced with permission from (**a**) ref. [142] Copyright (2020), American Chemical Society; (**b**) ref. [143] Copyright (2021), American Chemical Society; (**d**) ref. [146] Copyright (2023), John Wiley and Sons; (**e**) ref. [147] Copyright (2024), John Wiley and Sons; (**f**) ref. [149] Copyright (2022), John Wiley and Sons; (**g**) ref. [150] Copyright (2023), Springer Nature.

3.4.2. Direct Methanol Fuel Cells

Direct methanol fuel cells (DMFCs) have attracted extensive research attention from scientists worldwide due to their notable advantages, including potentially high efficiency, simple design, direct internal fuel conversion, and convenient refueling. However, methanol crossover through the ion exchange membrane to the cathode not only reduces methanol utilization efficiency but also leads to a substantial increase in oxygen electrode polarization, thereby degrading DMFC performance. Consequently, developing proton exchange membranes capable of significantly suppressing methanol permeability is imperative [154,155]. However, direct application of 2D materials in fuel cells faces technical bottlenecks, often necessitating polymer composite approaches. For example, NH_2-functionalized graphdiyne (NH_2-GDY), synthesized from 2,4,6-triacetylaniline monomers,

was compounded with Nafion to fabricate NH_2-GDY@Nafion membranes. The inherent nanopores in NH_2-GDY provided sufficiently large channels for selective proton transport, while amino groups enhanced interfacial compatibility with Nafion through acid-base pairing. At 80 °C in 1 M methanol solution, the NH_2-GDY@Nafion membrane achieved a maximum power density of 42.5 mW cm^{-2}. This composite reduced Nafion consumption by 58% while outperforming pure Nafion [156]. Building on this, a nitrogen-rich GDY composite membrane (3NGDY-Nafion) was developed. Single-layer 3NGDY can reduce methanol permeation by 43%, while the value of double-layer 3NGDY can reach as high as 69%. The high nitrogen content strengthened interfacial effects, further enhancing both proton conductivity and methanol barrier properties. Under operational conditions at 65 °C, it achieved a maximum power density of 80.48 mW cm^{-2} (Figure 12a), significantly surpassing the performance of commercial Nafion 212 membranes [157].

3.4.3. Vanadium Redox Flow Batteries

Flow batteries have evolved into critical large-scale electrochemical energy storage systems. Within these systems, the ion exchange membrane serves as an essential structural component that fulfills dual functions in terms of separating positive and negative electrolytes and selectively permitting ion permeation. This enables the prevention of self-discharge caused by crossover of active species between electrolytes and forms the completion of the battery circuit. Among various flow battery types [158], using all-vanadium flow batteries (VFBs) as an example, an ideal VFB membrane requires ultra-low vanadium ion permeability, exceptional chemical stability, high mechanical strength, superior ionic conductivity, and precise ion selectivity. These properties collectively ensure high battery efficiency, minimal water flux, and maintenance of electrolyte balance at both electrodes during charge/discharge cycles. Similarly, 2D materials provide innovative solutions for proton conduction membranes in vanadium redox flow batteries (VRFBs). For graphene oxide (GO), crosslinking strategies can engineer regular interlayer spacing to effectively sieve VO^{2+} ions. Kim et al. synthesized a graphene oxide framework (GOF) by crosslinking GO with ethylenediamine (EDA), achieving an effective pore size of 5.9 Å. This structure selectively blocked vanadium ions while permitting proton conduction, reducing VO^{2+} permeability to one-quarter of baseline membranes (Figure 12b) [159]. Alternatively, MoS_2 nanosheets as protective layers demonstrated reduced VO^{2+} permeability and enhanced chemical stability. These membranes achieved 80% energy efficiency at 200 mA cm^{-2} and maintained stability over nearly 800 cycles (Figure 12d) [160]. For covalent organic frameworks (COFs), fabricating freestanding thin membranes with high crystallinity and regular pores remains challenging. Xu et al. addressed this using sulfonated poly(ether ether ketone) (SPEEK) as a crystallization mediator. The -SO_3H groups of SPEEK templated COF precursor assembly, inducing ordered crystallization. Resulting freestanding COF membranes exhibited highly ordered nanopores and achieved proton conductivity of 75 mS cm^{-1} (Figure 12c), enabling excellent VRFB performance at room temperature and 100% RH [66].

Further advancing this approach, interlacing sulfonated COFs (SCOFs) with Nafion yielded self-supporting continuous membranes. The resulting wedge–tenon reinforcement structure narrowed pore apertures from 15.0 Å to 5–10 Å, enhancing H^+/V^{n+} selectivity. Simultaneously, crystalline-ordered -SO_3H groups created efficient proton-hopping pathways, achieving 143.9 mS cm^{-1} conductivity at 80 °C (Figure 12e) [161]. This work demonstrates the functional advantages of 2D-ordered crystalline materials in VRFB applications.

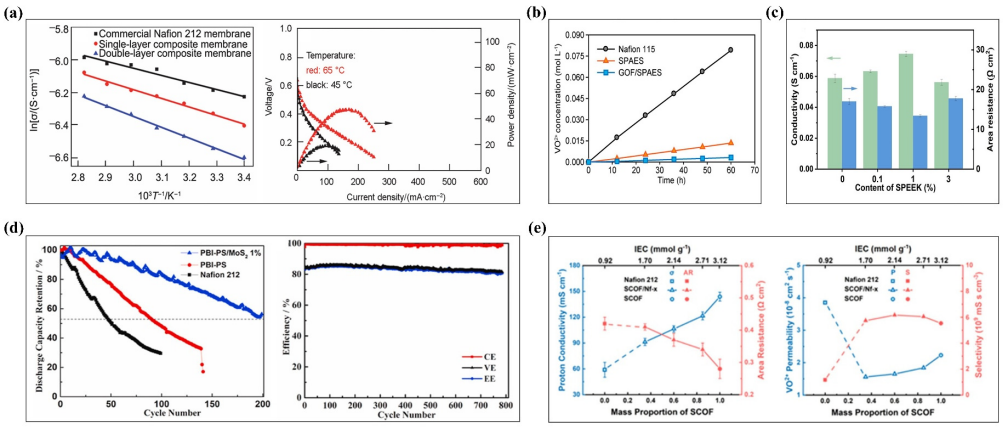

Figure 12. (**a**) The variation in proton conductivity with temperature in 3NGDY composite Nafion 212 membranes. Polarization curve and power density of 3NGDY composite Nafion 212 membranes [158]. (**b**) Changes in VO^{2+} ion concentration over time in blank solution in diffusion pool [159]. (**c**) Conductivity and area resistance of TpPa-SO_3H/SPEEK-x% membrane [66]. (**d**) Capacity retention rates of Nafion 212, PBI-PS, and PBI-PS/MoS_2 1% membranes. Cycle performance of PBI-PS/MoS_2 1% battery [160]. (**e**) Proton conductivity (σ) and area resistance. VO^{2+} permeability and H^+/V^{n+} ion selectivity [161]. Reproduced with permission from (**b**) ref. [159] Copyright (2018), American Chemical Society; (**d**) ref. [160] Copyright (2021), Elsevier; (**e**) ref. [161] Copyright (2024), Elsevier.

Table 1. A comparison of part advanced 2D membranes and their performance in different applications.

Membranes	Technology	Mechanism	Test conditions	Performance	Ref.
Desalination Seawater					
AD-rGO	Nanofiltration	Size sieving	Water/NaCl	Water permeability: 2647 L m^{-2} h^{-1} bar^{-1}; Salt rejection: 99.0%	[102]
ArGO-PSSNa	Forward Osmosis	Electrostatic repulsion	Water/NaCl	Water permeability: 47.0 L m^{-2} h^{-1}; Salt rejection: 99.7%	[104]
	Nanofiltration	Electrostatic repulsion	Water/NaCl	Water permeability: 48.6 L m^{-2} h^{-1} Salt rejection: 99.5%	
GDY@PCHF	Vacuum Membrane Distillation	Size sieving	Water/NaCl	Water permeability: 700 L m^{-2} h^{-1}; Salt rejection: 99.9%	[106]
c-GDY	Nanofiltration	Size sieving	Water/NaCl	Water permeability: ~32.9 mol m^{-2} h^{-1} bar^{-1}; Salt rejection: 99.7%	[107]
NoN membranes	Nanofiltration	Size sieving	Water/Mg_2SO_4	Water permeability: 30.0 L m^{-2} h^{-1} bar^{-1}; Salt rejection: 99.0%	[109]
High-Value Ion Separation					
CMP-masked porous graphene	Electric field-driven	Size sieving	K^+, Na^+, Li^+, Ca^{2+}, Mg^{2+}	Selectivity: K^+/Na^+ = 20, K^+/Mg^{2+} = 330; Li^+/divalent ions > 900	[115]
UHCD IEMs	Diffusion	Electrostatic repulsion	Na^+, Cl^-	Ionic conductivity enhance 4.5–13 times	[116]
M-SAT membranes	Diffusion Nanofiltration	Size sieving Electrostatic repulsion	H^+, Fe^{2+} Water/Na_2SO_4	Selectivity: H^+/Fe^{2+} > 800 Salt rejection: 100%	[117]
i-GO	Diffusion	Biological ion channel	K^+, Ca^{2+}, Mg^{2+}, Fe^{3+}, Cu^{2+}	Permeability: K^+ 1.36 mol m^{-2} h^{-1} Selectivity: K^+/Mg^{2+} = 9.11; K^+/Ca^{2+} = 6.44; K^+/Cu^{2+} = 8.93; K^+/Fe^{3+} = 28.29	[119]
Functionalized Graphene	Electric field-driven	Biological ion channel	H^+, K^+, Li^+, Na^+, Cs^+, Cl^-	K^+/Li^+ =48.6;K^+/Cl^- ≈ 76; H^+/Cl^- ≈ 59.3; Li^+/Cl^- ≈ 36	[120]
Nanopores COF-cys	Diffusion	pH response	K^+, Na^+	Selectivity: K^+/Na^+ = 1.7 (pH 3.8); Na^+/K^+ = 2.9 (pH 8.9)	[122]

Table 1. *Cont.*

Desalination Seawater					
Membranes	Technology	Mechanism	Test conditions	Performance	Ref.
Osmotic Energy Conversion					
GPPS membranes	Reverse electrodialysis	Size sieving; Electrostatic repulsion	0.5 M NaCl; 0.01 M NaCl	Max power density: 13.8 W m^{-2}	[125]
HGN membranes	Reverse electrodialysis	Size sieving Electrostatic repulsion	1 M KCl; 0.001M KCl	Power density: >100 W m^{-2}	[126]
MoS_2 membranes	Reverse electrodialysis	Size sieving	0.5 M NaCl; 0.1 M NaCl; 0.0 1M NaCl	Max Power density: 6.7 W m^{-2}	[127]
MXene-PPS	Reverse electrodialysis	Size sieving Electrostatic repulsion	0.5 M NaCl; 0.01 M NaCl	Power density: 1.57 W m^{-2}	[128]
MXene/PBONF	Reverse electrodialysis	Size sieving Electrostatic repulsion	0.5 M NaCl; 0.01 M NaCl	Selectivity: Na^+/Cl^- 0.87 Power density: 15.7 W m^{-2}	[132]
MXene/ZIF-8	Reverse electrodialysis	Size sieving Electrostatic repulsion Nano confined	0.5 M NaCl; 0.01 M NaCl 0.5 M NaCl; 0.001 M NaCl	Selectivity: Na^+/Cl^- 0.906 Max Power density: 48.05 W m^{-2}	[133]
MXene/PS-b-P2VP	Reverse electrodialysis	Size sieving pH response	0.1 M KCl; 0.5 M NaCl 0.01 M NaCl	Max Power density: 6.74 W m^{-2}	[134]
C_3N_4/MXene/CEL	Reverse electrodialysis	Photothermal drive	0.5 M NaCl 0.01 M NaCl	Power density: 1.68 W m^{-2}	[137]
Cu-TCPP membranes	Reverse electrodialysis	Size sieving Electrostatic repulsion Photothermal drive	0.5 M NaCl 0.01 M NaCl	Power density: 16.64 W m^{-2}	[138]
Proton Conductivity					
NGMs membranes	Transmembrane conductivity testing	Nitrogen-doped	1M HCl	Proton conductivity: 1.4 × 10^5 S m^{-2}	[143]
Titania	Transmembrane conductivity testing	Titanium vacancy	0.1M–1M HCl at 260 °C	Max proton conductivity: 200 S cm^{-1}	[144]
GDY	Transmembrane conductivity testing	Grotthuss	water vapor at rt.	Proton conductivity: 5.1 × 10^3 S cm^{-1}	[147]
GDYO	Au forked electrode testing	hydrogen-bond proton transport	100% RH 348 K	Proton conductivity: 0.54 S cm^{-1}	[149]
TpBd-SO_3H	Two electrode testing	hydrogen-bond proton transport	1M HCl 100% RH, 90 °C	Proton conductivity: 1389 mS cm^{-1}	[151]
TpBd-$(SO_3H)_2$ iCOFMs	Two-probe testing	hydrogen-bond proton transport Nano confined	100% RH, 90 °C	Proton conductivity: 0.66 S cm^{-1}	[152]
Direct Methanol Fuel Cell					
NH_2-GDY@Nafion	Two electrode testing DMFC testing	Grotthuss Vehicle	1 M Methanol solution at 80 °C	Power density: 42.5 mW cm^{-2}	[156]
3NGDY-Nafion	Two electrode testing DMFC testing	Grotthuss Vehicle	1 M Methanol solution at 65 °C	Power density: 80.48 mW cm^{-2}	[157]

Table 1. *Cont.*

Desalination Seawater					
Membranes	Technology	Mechanism	Test conditions	Performance	Ref.
Vanadium Redox Flow Batteries					
GOF/SPAES	VRFB testing	Size sieving Nano confined Grotthuss	80 mA cm^{-2} in VRFB	VO^{2+} permeability reduced 4 times compared to Nafion 115 EE: 89%	[159]
TpPa SO_3H/SPEEK	Two electrode testing VRFB testing	Size sieving Nano confined	40 mA cm^{-2} in VRFB; 100% RH 20 °C in H_2SO_4	Proton conductivity: 75 mS cm^{-1} EE: 81.0%	[66]
SCOF/Nf	Two electrode testing VRFB testing	Size sieving Electrostatic repulsion	100 mA cm^{-2} in VRFB; 25 °C	Proton conductivity: 143.9 mS cm^{-1} H^+/V_n^+ selectivity:9.25 × 10^9 mS s cm^{-3} EE: 85.5%	[161]

4. Conclusions and Perspectives

Owing to their unique advantages, 2D materials offer promising solutions to overcome the permeance–selectivity trade-off in transmembrane transport processes. This review focuses on the latest research progress concerning the prevailing preparation methods and potential applications of 2D material membranes. Various strategies for preparing 2D membranes were discussed and we highlighted the critical superiorities of these methods in terms of controlling thickness, repairing defects, optimizing nanochannel, tuning surface charge, enhancing physicochemical stability, and enabling large-scale fabrication. Subsequently, we specifically discuss the transport and separation mechanisms enabling high ion selectivity, based on evaluating the practical performance of 2D material membranes. In addition, some potential strategies for overcoming the trade-off effect are discussed, including size sieving, electrostatic repulsion, nanoconfinement effects, biomimetic channel design, and stimuli-responsive regulation. Despite demonstrating promising potential and significant progress, 2D material membranes remain in their early stages of development. When membrane thickness is reduced from the micrometer to the atomic scale, the fabrication and application of 2D material membranes face many challenges. These include physical challenges (e.g., equipment for scalable fabrication of large-area membranes), chemical challenges (e.g., precise structural design), and physicochemical challenges (e.g., transport mechanisms). Some following fundamental research aspects need to be prioritized for pursuing large-scale applications.

How to obtain high-quality 2D membrane materials with continuously tunable pore sizes and precisely controlled pore functionalities. Although significant progress has been made in membrane material synthesis methodologies, breakthroughs in the permeance–selectivity trade-off still require further innovation in synthetic approaches. For instance, pore-creation techniques must achieve precise controllability to enable high-density, highly uniform, and atomically precise control. Physical and chemical etching techniques may struggle to achieve the fabrication of atomic-scale high-flux pores, yet they can lay the theoretical foundation for ion-selective transport innovation in 2D membranes through modeling studies. Chemical synthesis methods are likely the primary route to achieving precise fabrication of high-flux, highly uniform pores. Examples include CVD for synthesizing single-layer COF and MOF materials, and solution-based methods for preparing large-area 2D GDY membranes.

Current preparation methods primarily focus on small-area 2D membrane materials for fundamental research, while technologies for producing larger-area membranes suitable for industrial applications remain underdeveloped and face a long development path. Taking the CVD method, which is currently one of the most advanced techniques for large-

area, few-layer controllable preparation of 2D materials, as an example, the challenges for large-scale production and application include precise control of membrane thickness, mechanical properties, defect management, and efficient transfer of membrane materials. Apparently, the transfer of atomic-thick 2D membrane is not a low-cost procedure for their application. Strategies developed for large-area single-layer graphene preparation and application can serve as a reference in this regard. Simultaneously, there is still a lack of techniques for creating and controlling atomic-level pores using chemical and physical methods. Clearly, the large-scale production of such 2D membrane materials remains incapable of reducing costs, and there is an urgent need to develop efficient pore-forming technologies suitable for large-scale applications.

The current literature reports a wide distribution of pore sizes in 2D materials, ranging from tens of nanometers down to a single nanometer, with only a few studies achieving sub-nanometer or even angstrom-scale dimensions. Ions do not exist in isolation; within the nanochannels, it should point out the influence of water molecules and hydrated radius in ion transport and selectivity. For different ion species, the ion-selective transport caused by the ion size, charge number, and pore properties should be deeply revealed. How can the size-sieving effect and confined transport achieve highly efficient selectivity for ions with similar dimensions?

Functional groups on these 2D materials should be precisely controlled and should have some innovation. Currently, the functional groups within the pores of 2D material membranes remain limited (e.g., carboxyl, sulfonic acid groups), and methods for their precise control are scarce. Pore functionalization that relies on weak van der Waals interactions often suffers from poor stability. Enriching the diversity of pore functional groups (e.g., incorporating phosphorus, boron, transition metals, etc.) is a critical challenge for scientists to address. More functionalities create the conditions for achieving high selectivity. This advancement would enable the innovations of biomimetic ion channels, intelligent nanochannels for next-generation membranes.

The transport mechanisms of ions through atomic-scale membranes differ significantly from those in traditional thick membranes, thus needing to prompt innovative theoretical frameworks. Within pores of identical size, it remains mysterious what distinct phenomena arise in the confined transport of ions through atomically thin monolayers compared to thick membranes and how experiments can elucidate these differences. For revealing the transport mechanism, it is challenging to characterize the variations in the atomic thick 2D material using in situ devices.

Author Contributions: Investigation, methodology, formal analysis, software, writing—original draft, Z.J.; investigation, data curation, software, S.Z.; software, formal analysis, J.X.; conceptualization, formal analysis, Y.L.; supervision, review and editing, Y.Z.; supervision, formal analysis, J.L.; writing—review and editing, supervision, project administration, funding acquisition, formal analysis, Z.Z. All authors have read and agreed to the published version of the manuscript.

Funding: This work was supported by the National Natural Science Foundation of China (No. 52172251), the National Program for Support of Top-notch Young Professionals of China, and the North China Electric Power University Start-up Fund.

Data availability Statement: Data will be made available on request.

Conflicts of Interest: The authors declare that they have no known competing financial interests or personal relationships that could have appeared to influence the work reported in this paper.

References

1. Zhou, Y. Worldwide carbon neutrality transition? Energy efficiency, renewable, carbon trading and advanced energy policies. *Energy Rev.* **2023**, *2*, 10026. [CrossRef]
2. Yan, G.; Kenway, S.J.; Lam, K.L.; Lant, P.A. Water-energy trajectories for urban water and wastewater reveal the impact of city strategies. *Appl. Energy* **2024**, *366*, 123292. [CrossRef]
3. Gao, W.; Wang, Z.; Duan, F.; Li, Y.; Shi, S.; Sun, Z.; Zhou, B.; Lv, L. Comprehensive assessment of membrane technology for typical water treatment processes: A critical review. *Desalination* **2025**, *614*, 119171. [CrossRef]
4. Ji, T.; Zhang, C.; Xiao, X.; Wang, Y.; Cao, D.; Adomkevicius, A.; Zhao, Y.; Sun, X.; Fu, K.; Zhu, H. High Ion Conductive and Selective Membrane Achieved through Dual Ion Conducting Mechanisms. *Small* **2023**, *19*, e2206807. [CrossRef]
5. Zhou, Z.; Shinde, D.B.; Guo, D.; Cao, L.; Al Nuaimi, R.; Zhang, Y.; Enakonda, L.R.; Lai, Z. Flexible Ionic Conjugated Microporous Polymer Membranes for Fast and Selective Ion Transport. *Adv. Funct. Mater.* **2021**, *32*, 2108672. [CrossRef]
6. Borah, D.; Hazarika, G.; Gogoi, A.; Goswami, S.; Sawake, S.V.; Yadav, D.; Karki, S.; Gohain, M.B.; Sahu, L.R.; Ingole, P.G. Polymeric membranes for sustainable gas separation: A comprehensive review with challenges, innovations and future perspectives. *Renew. Sustain. Energy Rev.* **2025**, *219*, 115868. [CrossRef]
7. Diao, X.; Zhang, X.; Li, Y.; Chen, X.; Zhao, Z.; Wang, P.; Liu, P.; Gao, H.; Wang, G. Heterogeneous network of 2D MOFs decorated 1D CNTs imparting multiple functionalities to composite phase change materials. *Nano Res. Energy* **2024**, *3*, e9120114. [CrossRef]
8. Li, Q.; Zhang, W.; Peng, J.; Zhang, W.; Liang, Z.; Wu, J.; Feng, J.; Li, H.; Huang, S. Metal–Organic Framework Derived Ultrafine Sb@Porous Carbon Octahedron via In Situ Substitution for High-Performance Sodium-Ion Batteries. *ACS Nano* **2021**, *15*, 15104–15113. [CrossRef]
9. Li, J.; Yi, Y.; Zuo, X.; Hu, B.; Xiao, Z.; Lian, R.; Kong, Y.; Tong, L.; Shao, R.; Sun, J.; et al. Graphdiyne/Graphene/Graphdiyne Sandwiched Carbonaceous Anode for Potassium-Ion Batteries. *ACS Nano* **2022**, *16*, 3163–3172. [CrossRef]
10. Ci, H.; Shi, Z.; Wang, M.; He, Y.; Sun, J. A review in rational design of graphene toward advanced Li–S batteries. *Nano Res. Energy* **2023**, *2*, e9120054. [CrossRef]
11. Gao, X.; Zhu, Y.; Yi, D.; Zhou, J.; Zhang, S.; Yin, C.; Ding, F.; Zhang, S.; Yi, X.; Wang, J.; et al. Ultrathin graphdiyne film on graphene through solution-phase van der Waals epitaxy. *Sci. Adv.* **2018**, *4*, eaat6378. [CrossRef] [PubMed]
12. Lim, K.R.G.; Shekhirev, M.; Wyatt, B.C.; Anasori, B.; Gogotsi, Y.; Seh, Z.W. Fundamentals of MXene synthesis. *Nat. Synth.* **2022**, *1*, 601–614. [CrossRef]
13. Li, J.; Zhao, N.; Liu, X.; Chang, X.; Zheng, W.; Zhang, J. Two-dimensional layered double hydroxides for advanced sensors. *Co-ord. Chem. Rev.* **2024**, *523*, 216262. [CrossRef]
14. Tian, X.; Ye, C.; Zhang, L.; Sugumar, M.K.; Zhao, Y.; McKeown, N.B.; Margadonna, S.; Tan, R. Enhancing Membrane Materials for Efficient Li Recycling and Recovery. *Adv. Mater.* **2024**, *37*, e2402335. [CrossRef]
15. Ali, A.; Tufa, R.A.; Macedonio, F.; Curcio, E.; Drioli, E. Membrane technology in renewable-energy-driven desalination. *Renew. Sustain. Energy Rev.* **2018**, *81*, 1–21. [CrossRef]
16. Yang, F.; Yong, M.; Li, Z.; Yang, Z.; Zhang, X. Breaking the trade-off between lithium purity and lithium recovery: A comprehensive mathematical modeling based on membrane structure-property-performance relationships. *Water Res.* **2025**, *281*, 123678. [CrossRef]
17. Shen, L.; Yi, M.; Japip, S.; Han, C.; Tian, L.; Lau, C.H.; Wang, Y. Breaking through permeability–selectivity trade-off of thin-film composite membranes assisted with crown ethers. *AIChE J.* **2021**, *67*, e17173. [CrossRef]
18. Kidambi, P.R.; Chaturvedi, P.; Moehring, N.K. Subatomic species transport through atomically thin membranes: Present and future applications. *Science* **2021**, *374*, eabd7687. [CrossRef]
19. Liu, G.; Jin, W.; Xu, N. Two-Dimensional-Material Membranes: A New Family of High-Performance Separation Membranes. *Angew. Chem. Int. Ed. Engl.* **2016**, *55*, 13384–13397. [CrossRef]
20. Wang, J.; Zhou, H.; Li, S.; Wang, L. Selective Ion Transport in Two-Dimensional Lamellar Nanochannel Membranes. *Angew. Chem. Int. Ed. Engl.* **2023**, *62*, e202218321. [CrossRef]
21. Jiao, Y.; Yang, C.; Zhang, W.; Wang, Q.; Zhao, C. A review on direct osmotic power generation: Mechanism and membranes. *Renew. Sustain. Energy Rev.* **2023**, *191*, 114078. [CrossRef]
22. Liu, L.; Cheng, Q. Mass transfer characteristic research on electrodialysis for desalination and regeneration of solution: A comprehensive review. *Renew. Sustain. Energy Rev.* **2020**, *134*, 110115. [CrossRef]
23. León, T.; López, J.; Torres, R.; Grau, J.; Jofre, L.; Cortina, J.-L. Time-dependent 2-D model for transport of species analysis in electrodialysis: Concentration profiles and fluxes. *Desalination* **2023**, *565*, 116819. [CrossRef]
24. Kang, Y.; Xia, Y.; Wang, H.; Zhang, X. 2D Laminar Membranes for Selective Water and Ion Transport. *Adv. Funct. Mater.* **2019**, *29*, 1902014. [CrossRef]
25. Luo, J.; Qiao, R.; Ding, B. Enhancement of ion selectivity and permeability in two-dimensional material membranes. *Matter* **2024**, *7*, 3351–3389. [CrossRef]
26. Yu, X.; Ren, W. Ion and Water Transport in 2D Nanofluidic Channels. *Adv. Funct. Mater.* **2024**, *34*, 2313968. [CrossRef]

27. Wang, S.; Yang, L.; He, G.; Shi, B.; Li, Y.; Wu, H.; Zhang, R.; Nunes, S.; Jiang, Z. Two-dimensional nanochannel membranes for molecular and ionic separations. *Chem. Soc. Rev.* **2020**, *49*, 1071–1089. [CrossRef]
28. Kang, Y.; Wang, Y.; Zhang, H.; Wang, Z.; Zhang, X.; Wang, H. Functionalized 2D membranes for separations at the 1-nm scale. *Chem. Soc. Rev.* **2024**, *53*, 7939–7959. [CrossRef]
29. Cui, Y.; Gao, L.; Ying, C.; Tian, J.; Liu, Z. Two-Dimensional Material-Based Nanofluidic Devices and Their Applications. *ACS Nano* **2025**, *19*, 1911–1943. [CrossRef]
30. Tiwary, S.K.; Singh, M.; Chavan, S.V.; Karim, A. Graphene oxide-based membranes for water desalination and purification. *npj 2D Mater. Appl.* **2024**, *8*, 27. [CrossRef]
31. Gu, P.; Liu, S.; Cheng, X.; Zhang, S.; Wu, C.; Wen, T.; Wang, X. Recent strategies, progress, and prospects of two-dimensional metal carbides (MXenes) materials in wastewater purification: A review. *Sci. Total. Environ.* **2023**, *912*, 169533. [CrossRef] [PubMed]
32. Novoselov, K.S.; Fal'Ko, V.I.; Colombo, L.; Gellert, P.R.; Schwab, M.G.; Kim, K. A roadmap for graphene. *Nature* **2012**, *490*, 192–200. [CrossRef] [PubMed]
33. Asif, M.B.; Iftekhar, S.; Maqbool, T.; Pramanik, B.K.; Tabraiz, S.; Sillanpää, M.; Zhang, Z. Two-dimensional nanoporous and lamellar membranes for water purification: Reality or a myth? *Chem. Eng. J.* **2022**, *432*, 134335. [CrossRef]
34. Zhang, H.; Li, X.; Hou, J.; Jiang, L.; Wang, H. Angstrom-scale ion channels towards single-ion selectivity. *Chem. Soc. Rev.* **2022**, *51*, 2224–2254. [CrossRef]
35. Xin, W.; Jiang, L.; Wen, L. Two-Dimensional Nanofluidic Membranes toward Harvesting Salinity Gradient Power. *Acc. Chem. Res.* **2021**, *54*, 4154–4165. [CrossRef]
36. Zhu, L.; Cao, Y.; Xu, T.; Yang, H.; Wang, L.; Dai, L.; Pan, F.; Chen, C.; Si, C. Covalent organic framework membranes for energy storage and conversion. *Energy Environ. Sci.* **2025**, *18*, 5675–5739. [CrossRef]
37. Senila, L.; Kovacs, E.; Senila, M. A Review of Polylactic Acid (PLA) and Poly(3-hydroxybutyrate) (PHB) as Bio-Sourced Polymers for Membrane Production Applications. *Membranes* **2025**, *15*, 210. [CrossRef]
38. Cai, Z.; Liu, B.; Zou, X.; Cheng, H.-M. Chemical Vapor Deposition Growth and Applications of Two-Dimensional Materials and Their Heterostructures. *Chem. Rev.* **2018**, *118*, 6091–6133. [CrossRef]
39. Luo, L.; Hou, L.; Cui, X.; Zhan, P.; He, P.; Dai, C.; Li, R.; Dong, J.; Zou, Y.; Liu, G.; et al. Self-condensation-assisted chemical vapour deposition growth of atomically two-dimensional MOF single-crystals. *Nat. Commun.* **2024**, *15*, 3618. [CrossRef]
40. Baek, K.; Yun, G.; Kim, Y.; Kim, D.; Hota, R.; Hwang, I.; Xu, D.; Ko, Y.H.; Gu, G.H.; Suh, J.H.; et al. Free-Standing, Single-Monomer-Thick Two-Dimensional Polymers through Covalent Self-Assembly in Solution. *J. Am. Chem. Soc.* **2013**, *135*, 6523–6528. [CrossRef]
41. Huo, C.; Yan, Z.; Song, X.; Zeng, H. 2D materials via liquid exfoliation: A review on fabrication and applications. *Sci. Bull.* **2015**, *60*, 1994–2008. [CrossRef]
42. Cun, H.; Miao, Z.; Hemmi, A.; Al-Hamdani, Y.; Iannuzzi, M.; Osterwalder, J.; Altman, M.S.; Greber, T. High-Quality Hexagonal Boron Nitride from 2D Distillation. *ACS Nano* **2020**, *15*, 1351–1357. [CrossRef]
43. Liu, H.; Zhang, T.; Wu, P.; Lee, H.W.; Liu, Z.; Tang, T.W.; Tang, S.-Y.; Kang, T.; Park, J.-H.; Wang, J.; et al. Boosting Monolayer Transition Metal Dichalcogenides Growth by Hydrogen-Free Ramping during Chemical Vapor Deposition. *Nano Lett.* **2024**, *24*, 8277–8286. [CrossRef]
44. Rubio-Giménez, V.; Arnauts, G.; Wang, M.; Mata, E.S.O.; Huang, X.; Lan, T.; Tietze, M.L.; Kravchenko, D.E.; Smets, J.; Wauteraerts, N.; et al. Chemical Vapor Deposition and High-Resolution Patterning of a Highly Conductive Two-Dimensional Coordination Polymer Film. *J. Am. Chem. Soc.* **2022**, *145*, 152–159. [CrossRef] [PubMed]
45. Liu, J.; Fu, S.; Fu, Y.; Chen, Y.; Tadayon, K.; Hambsch, M.; Pohl, D.; Yang, Y.; Müller, A.; Zhao, F.; et al. Ammonia-Assisted Chemical Vapor Deposition Growth of Two-Dimensional Conjugated Coordination Polymer Thin Films. *J. Am. Chem. Soc.* **2025**, *147*, 18190–18196. [CrossRef] [PubMed]
46. Xiao, K.; Giusto, P.; Wen, L.; Jiang, L.; Antonietti, M. Nanofluidic Ion Transport and Energy Conversion through Ultrathin Free-Standing Polymeric Carbon Nitride Membranes. *Angew. Chem. Int. Ed. Engl.* **2018**, *57*, 10123–10126. [CrossRef]
47. Wetzl, C.; Silvestri, A.; Garrido, M.; Hou, H.; Criado, A.; Prato, M. The Covalent Functionalization of Surface-Supported Graphene: An Update. *Angew. Chem. Int. Ed. Engl.* **2022**, *62*, e202212857. [CrossRef] [PubMed]
48. Park, J.; Bhoyate, S.; Kim, Y.-H.; Lee, Y.H.; Conlin, P.; Cho, K.; Choi, W. Unusually High Ion Conductivity in Large-Scale Patternable Two-Dimensional MoS_2 Film. *ACS Nano* **2021**, *15*, 12267–12275. [CrossRef]
49. Kutagulla, S.; Carmichael, P.; Coupin, M.; Mutyala, D.; Ignacio, N.; Le, N.H.; Bohn, I.T.C.; Kim, J.-W.; Mason, K.S.; Warner, J.; et al. Ozonated Monolayer Graphene for Extended Performance and Durability in Hydrogen Fuel Cell Electric Vehicles. *ACS Nano* **2025**, *19*, 9422–9431. [CrossRef]
50. Li, G.; Li, Y.; Liu, H.; Guo, Y.; Li, Y.; Zhu, D. Architecture of graphdiyne nanoscale films. *Chem. Commun.* **2010**, *46*, 3256–3258. [CrossRef]
51. Zhou, J.; Gao, X.; Liu, R.; Xie, Z.; Yang, J.; Zhang, S.; Zhang, G.; Liu, H.; Li, Y.; Zhang, J.; et al. Synthesis of Graphdiyne Nanowalls Using Acetylenic Coupling Reaction. *J. Am. Chem. Soc.* **2015**, *137*, 7596–7599. [CrossRef] [PubMed]

52. Zhou, Z.; Tan, Y.; Yang, Q.; Bera, A.; Xiong, Z.; Yagmurcukardes, M.; Kim, M.; Zou, Y.; Wang, G.; Mishchenko, A.; et al. Gas permeation through graphdiyne-based nanoporous membranes. *Nat. Commun.* **2022**, *13*, 4031. [CrossRef] [PubMed]
53. Gao, X.; Zhou, J.; Du, R.; Xie, Z.; Deng, S.; Liu, R.; Liu, Z.; Zhang, J. Robust Superhydrophobic Foam: A Graphdiyne-Based Hierarchical Architecture for Oil/Water Separation. *Adv. Mater.* **2015**, *28*, 168–173. [CrossRef]
54. Matsuoka, R.; Sakamoto, R.; Hoshiko, K.; Sasaki, S.; Masunaga, H.; Nagashio, K.; Nishihara, H. Crystalline Graphdiyne Nanosheets Produced at a Gas/Liquid or Liquid/Liquid Interface. *J. Am. Chem. Soc.* **2017**, *139*, 3145–3152. [CrossRef] [PubMed]
55. Lu, C.; Yang, Y.; Wang, J.; Fu, R.; Zhao, X.; Zhao, L.; Ming, Y.; Hu, Y.; Lin, H.; Tao, X.; et al. High-performance graphdiyne-based electrochemical actuators. *Nat. Commun.* **2018**, *9*, 752. [CrossRef]
56. Wang, L.; Han, Y.; Xie, M.; Li, X.; Chen, Q.; Tang, Y.; Liu, Y.; Ge, H.; Li, H.; Cai, L.; et al. Synthesis of Hexabenzocoronene-Cored Graphdiyne Nanosheets through Dehydrogenative Coupling on Au(111) Surface. *Angew. Chem. Int. Ed. Engl.* **2024**, *63*, e202411722. [CrossRef]
57. Kaliya, K.; Bhardwaj, N.; Ruchika; Saneja, A. An Imine-Based Two-Dimensional Covalent Organic Framework for Gemcitabine Delivery. *Colloids Interfaces* **2025**, *9*, 8. [CrossRef]
58. Liu, K.; Qi, H.; Dong, R.; Shivhare, R.; Addicoat, M.; Zhang, T.; Sahabudeen, H.; Heine, T.; Mannsfeld, S.; Kaiser, U.; et al. On-water surface synthesis of crystalline, few-layer two-dimensional polymers assisted by surfactant monolayers. *Nat. Chem.* **2019**, *11*, 994–1000. [CrossRef]
59. Ying, Y.; Tong, M.; Ning, S.; Ravi, S.K.; Peh, S.B.; Tan, S.C.; Pennycook, S.J.; Zhao, D. Ultrathin Two-Dimensional Membranes Assembled by Ionic Covalent Organic Nanosheets with Reduced Apertures for Gas Separation. *J. Am. Chem. Soc.* **2020**, *142*, 4472–4480. [CrossRef]
60. Liu, X.; Lin, W.; Al Mohawes, K.B.; Khashab, N.M. Ultrahigh Proton Selectivity by Assembled Cationic Covalent Organic Framework Nanosheets. *Angew. Chem. Int. Ed. Engl.* **2024**, *64*, e202419034. [CrossRef]
61. Khan, N.A.; Zhang, R.; Wu, H.; Shen, J.; Yuan, J.; Fan, C.; Cao, L.; Olson, M.A.; Jiang, Z. Solid–Vapor Interface Engineered Covalent Organic Framework Membranes for Molecular Separation. *J. Am. Chem. Soc.* **2020**, *142*, 13450–13458. [CrossRef]
62. Qian, Y.; Wu, Y.; Qiu, S.; He, X.; Liu, Y.; Kong, X.; Tian, W.; Jiang, L.; Wen, L. A Bioinspired Free-Standing 2D Crown-Ether-Based Polyimine Membrane for Selective Proton Transport. *Angew. Chem. Int. Ed. Engl.* **2023**, *62*, e202300167. [CrossRef]
63. Zhang, N.; Wang, T.; Wu, X.; Jiang, C.; Zhang, T.; Jin, B.; Ji, H.; Bai, W.; Bai, R. From 1D Polymers to 2D Polymers: Preparation of Free-Standing Single-Monomer-Thick Two-Dimensional Conjugated Polymers in Water. *ACS Nano* **2017**, *11*, 7223–7229. [CrossRef] [PubMed]
64. Wei, S.; Zhang, F.; Zhang, W.; Qiang, P.; Yu, K.; Fu, X.; Wu, D.; Bi, S. Semiconducting 2D Triazine-Cored Covalent Organic Frameworks with Unsubstituted Olefin Linkages. *J. Am. Chem. Soc.* **2019**, *141*, 14272–14279. [CrossRef] [PubMed]
65. Zhang, Y.; Guo, J.; Han, G.; Bai, Y.; Ge, Q.; Ma, J.; Lau, C.H.; Shao, L. Molecularly soldered covalent organic frameworks for ultrafast precision sieving. *Sci. Adv.* **2021**, *7*, eabe8706. [CrossRef] [PubMed]
66. Wu, Y.; Wang, Y.; Zhang, D.; Xu, F.; Dai, L.; Qu, K.; Cao, H.; Xia, Y.; Li, S.; Huang, K.; et al. Crystallizing Self-Standing Covalent Organic Framework Membranes for Ultrafast Proton Transport in Flow Batteries. *Angew. Chem. Int. Ed. Engl.* **2023**, *62*, e202313571. [CrossRef]
67. Shi, B.; Pang, X.; Lyu, B.; Wu, H.; Shen, J.; Guan, J.; Wang, X.; Fan, C.; Cao, L.; Zhu, T.; et al. Spacer-Engineered Ionic Channels in Covalent Organic Framework Membranes toward Ultrafast Proton Transport. *Adv. Mater.* **2023**, *35*, e2211004. [CrossRef]
68. Pang, X.; Shi, B.; Liu, Y.; Li, Y.; Zhang, Y.; Wang, T.; Xu, S.; Wang, X.; Liu, Z.; Xing, N.; et al. Phosphorylated Covalent Organic Framework Membranes Toward Ultrafast Single Lithium-Ion Transport. *Adv. Mater.* **2024**, *36*, e2413022. [CrossRef]
69. You, X.; Wu, H.; Zhang, R.; Su, Y.; Cao, L.; Yu, Q.; Yuan, J.; Xiao, K.; He, M.; Jiang, Z. Metal-coordinated sub-10 nm membranes for water purification. *Nat. Commun.* **2019**, *10*, 4160. [CrossRef]
70. Li, R.; Yao, Z.; Li, Z.; Liao, L.; Sun, H.; Cong, C.; Huang, X.; Wu, K.; Wang, T.; Tian, H.; et al. Mechanical exfoliation of non-layered metal oxides into ultrathin flakes. *Nat. Synth.* **2024**, *4*, 106–115. [CrossRef]
71. Tian, W.; Kang, M.-A.; Shakya, J.; Li, Q.; Sui, X.; Liu, M.; Wang, H.; Hamedi, M.M. Liquid-phase exfoliation of 2D transition metal dichalcogenide nanosheets in water. *Chem. Eng. J.* **2025**, *513*, 162587. [CrossRef]
72. Yang, R.; Mei, L.; Zhang, Q.; Fan, Y.; Shin, H.S.; Voiry, D.; Zeng, Z. High-yield production of mono- or few-layer transition metal dichalcogenide nanosheets by an electrochemical lithium ion intercalation-based exfoliation method. *Nat. Protoc.* **2022**, *17*, 358–377. [CrossRef]
73. Zou, Y.-C.; Mogg, L.; Clark, N.; Bacaksiz, C.; Milovanovic, S.; Sreepal, V.; Hao, G.-P.; Wang, Y.-C.; Hopkinson, D.G.; Gorbachev, R.; et al. Ion exchange in atomically thin clays and micas. *Nat. Mater.* **2021**, *20*, 1677–1682. [CrossRef] [PubMed]
74. Alhabeb, M.; Maleski, K.; Mathis, T.S.; Sarycheva, A.; Hatter, C.B.; Uzun, S.; Levitt, A.; Gogotsi, Y. Selective Etching of Silicon from Ti_3SiC_2 (MAX) To Obtain 2D Titanium Carbide (MXene). *Angew. Chem. Int. Ed. Engl.* **2018**, *57*, 5444–5448. [CrossRef] [PubMed]
75. Wu, J.; Lin, H.; Moss, D.J.; Loh, K.P.; Jia, B. Graphene oxide for photonics, electronics and optoelectronics. *Nat. Rev. Chem.* **2023**, *7*, 162–183. [CrossRef] [PubMed]

76. Herrera-Velarde, S.; Euán-Díaz, E.C.; Castañeda-Priego, R. Ordering and Dynamics of Interacting Colloidal Particles under Soft Confinement. *Colloids Interfaces* **2021**, *5*, 29. [CrossRef]
77. Kruk, T.; Warszyński, P. Conductive Nanofilms with Oppositely Charged Reduced Graphene Oxides as a Base for Electroactive Coatings and Sensors. *Colloids Interfaces* **2021**, *5*, 20. [CrossRef]
78. Kiran, P.S.; Prasad, S.; Satish, C.; Indupuri, S.; Kumar, K.V.; Keshri, S.; Keshri, A.K. Breaking Strong Lip to Lip Interactions in Hexagonal Boron Nitride: A Facile, Scalable Exfoliation Protocol. *Small* **2025**, *21*, e2504831. [CrossRef]
79. Lu, X.; Gabinet, U.R.; Ritt, C.L.; Feng, X.; Deshmukh, A.; Kawabata, K.; Kaneda, M.; Hashmi, S.M.; Osuji, C.O.; Elimelech, M. Relating Selectivity and Separation Performance of Lamellar Two-Dimensional Molybdenum Disulfide (MoS_2) Membranes to Nanosheet Stacking Behavior. *Environ. Sci. Technol.* **2020**, *54*, 9640–9651. [CrossRef]
80. Ventura-Martinez, K.; Zhu, Y.; Booth, A.; Hatzell, K.B. Impact of Asymmetric Microstructure on Ion Transport in $Ti_3C_2T_x$ Membranes. *Nano Lett.* **2024**, *24*, 13551–13557. [CrossRef]
81. Huang, Y.; Pan, Y.-H.; Yang, R.; Bao, L.-H.; Meng, L.; Luo, H.-L.; Cai, Y.-Q.; Liu, G.-D.; Zhao, W.-J.; Zhou, Z.; et al. Universal mechanical exfoliation of large-area 2D crystals. *Nat. Commun.* **2020**, *11*, 2453. [CrossRef] [PubMed]
82. Moon, J.-Y.; Kim, M.; Kim, S.-I.; Xu, S.; Choi, J.-H.; Whang, D.; Watanabe, K.; Taniguchi, T.; Park, D.S.; Seo, J.; et al. Layer-engineered large-area exfoliation of graphene. *Sci. Adv.* **2020**, *6*, eabc6601. [CrossRef] [PubMed]
83. Bai, Y.; Xu, Y.; Sun, L.; Ward, Z.; Wang, H.; Ratnayake, G.; Wang, C.; Zhao, M.; He, H.; Gao, J.; et al. Two-dimensional Nanosheets by Liquid Metal Exfoliation. *Adv. Mater.* **2024**, *37*, e2416375. [CrossRef] [PubMed]
84. Ritt, C.L.; Werber, J.R.; Deshmukh, A.; Elimelech, M. Monte Carlo Simulations of Framework Defects in Layered Two-Dimensional Nanomaterial Desalination Membranes: Implications for Permeability and Selectivity. *Environ. Sci. Technol.* **2019**, *53*, 6214–6224. [CrossRef]
85. Nicklin, C. Capturing Surface Processes. *Science* **2014**, *343*, 739–740. [CrossRef]
86. Chen, L.; Shi, G.; Shen, J.; Peng, B.; Zhang, B.; Wang, Y.; Bian, F.; Wang, J.; Li, D.; Qian, Z.; et al. Ion sieving in graphene oxide membranes via cationic control of interlayer spacing. *Nature* **2017**, *550*, 380–383. [CrossRef]
87. Paton, K.R.; Varrla, E.; Backes, C.; Smith, R.J.; Khan, U.; O'Neill, A.; Boland, C.S.; Lotya, M.; Istrate, O.M.; King, P.; et al. Scalable production of large quantities of defect-free few-layer graphene by shear exfoliation in liquids. *Nat. Mater.* **2014**, *13*, 624–630. [CrossRef]
88. Islam, A.; Mukherjee, B.; Pandey, K.K.; Keshri, A.K. Ultra-Fast, Chemical-Free, Mass Production of High Quality Exfoliated Graphene. *ACS Nano* **2021**, *15*, 1775–1784. [CrossRef]
89. Wang, N.; Yang, G.; Wang, H.; Yan, C.; Sun, R.; Wong, C.-P. A universal method for large-yield and high-concentration exfoliation of two-dimensional hexagonal boron nitride nanosheets. *Mater. Today* **2019**, *27*, 33–42. [CrossRef]
90. Pendse, A.; Cetindag, S.; Wang, K.; Li, D.; Castellano, R.J.; Yang, D.-C.; Wang, T.; Shan, J.W.; Kim, S. Intrinsic ion transport of highly charged sub-3-nm boron nitride nanotubes. *Mater. Today* **2022**, *60*, 79–90. [CrossRef]
91. Hu, C.Y.; Achari, A.; Rowe, P.; Xiao, H.; Suran, S.; Li, Z.; Huang, K.; Chi, C.; Cherian, C.T.; Sreepal, V.; et al. pH-dependent water permeability switching and its memory in MoS2 membranes. *Nature* **2023**, *616*, 719–723. [CrossRef]
92. Ries, L.; Petit, E.; Michel, T.; Diogo, C.C.; Gervais, C.; Salameh, C.; Bechelany, M.; Balme, S.; Miele, P.; Onofrio, N.; et al. Enhanced sieving from exfoliated MoS2 membranes via covalent functionalization. *Nat. Mater.* **2019**, *18*, 1112–1117. [CrossRef]
93. Kim, C.; Koh, D.-Y.; Lee, Y.; Choi, J.; Cho, H.S.; Choi, M. Bottom-up synthesis of two-dimensional carbon with vertically aligned ordered micropores for ultrafast nanofiltration. *Sci. Adv.* **2023**, *9*, eade7871. [CrossRef]
94. Yi, M.; Wang, M.; Wang, Y.; Wang, Y.; Chang, J.; Kheirabad, A.K.; He, H.; Yuan, J.; Zhang, M. Poly(ionic liquid)-Armored MXene Membrane: Interlayer Engineering for Facilitated Water Transport. *Angew. Chem. Int. Ed. Engl.* **2022**, *61*, e202202515. [CrossRef]
95. Liu, L.; Orbay, M.; Luo, S.; Duluard, S.; Shao, H.; Harmel, J.; Rozier, P.; Taberna, P.-L.; Simon, P. Exfoliation and Delamination of $Ti_3C_2T_x$ MXene Prepared via Molten Salt Etching Route. *ACS Nano* **2021**, *16*, 111–118. [CrossRef]
96. Xia, Z.; Chen, W.; Shevate, R.; Wang, Y.; Gao, F.; Wang, D.; Kazi, O.A.; Mane, A.U.; Lee, S.S.; Elam, J.W.; et al. Tunable Ion Transport with Freestanding Vermiculite Membranes. *ACS Nano* **2022**, *16*, 18266–18273. [CrossRef] [PubMed]
97. Wang, Z.; Yang, J.; Yong, M.; Zeng, X.; Tebyetekerwa, M.; Sun, K.; Bie, C.; Xing, C.; Wang, H.; Andreeva, D.V.; et al. From Layered Crystals to Permselective Membranes: History, Fundamentals, and Opportunities. *Chem. Rev.* **2025**, *125*, 6753–6818. [CrossRef] [PubMed]
98. DuChanois, R.M.; Porter, C.J.; Violet, C.; Verduzco, R.; Elimelech, M. Membrane Materials for Selective Ion Separations at the Water–Energy Nexus. *Adv. Mater.* **2021**, *33*, 2101312. [CrossRef] [PubMed]
99. Liu, H.; Wang, H.; Zhang, X. Facile Fabrication of Freestanding Ultrathin Reduced Graphene Oxide Membranes for Water Purification. *Adv. Mater.* **2014**, *27*, 249–254. [CrossRef]
100. Wang, J.; Zhang, X.; Yu, Z.; Gao, Y.; Lu, Q.; Ma, C.; Liu, K.; Yuan, Q.; Yang, Y. Fast water transport and ionic sieving in ultrathin stacked nanoporous 2D membranes. *Natl. Sci. Rev.* **2025**, *12*, nwae482. [CrossRef]
101. Xu, W.L.; Fang, C.; Zhou, F.; Song, Z.; Liu, Q.; Qiao, R.; Yu, M. Self-Assembly: A Facile Way of Forming Ultrathin, High-Performance Graphene Oxide Membranes for Water Purification. *Nano Lett.* **2017**, *17*, 2928–2933. [CrossRef]

102. Han, C.; Jiang, J.; Mu, L.; Zhao, W.; Liu, J.; Lan, J.; Hu, S.; Yang, H.; Gao, S.; Zhou, F.; et al. Quasi-vertically asymmetric channels of graphene oxide membrane for ultrafast ion sieving. *Nat. Commun.* **2025**, *16*, 1020. [CrossRef]
103. Li, Y.; Zhao, J.; Zhang, J.; Gong, X.; Zhou, J.; Zhang, N.; Su, Y. Smart and solvent-switchable graphene-based membrane for graded molecular sieving. *Nat. Commun.* **2025**, *16*, 5363. [CrossRef] [PubMed]
104. Zhang, H.; Xing, J.; Wei, G.; Wang, X.; Chen, S.; Quan, X. Electrostatic-induced ion-confined partitioning in graphene nanolaminate membrane for breaking anion–cation co-transport to enhance desalination. *Nat. Commun.* **2024**, *15*, 4324. [CrossRef] [PubMed]
105. Liu, Y.; Wang, Y.; Sengupta, B.; Kazi, O.A.; Martinson, A.B.F.; Elam, J.W.; Darling, S.B. Pillared Laminar Vermiculite Membranes with Tunable Monovalent and Multivalent Ion Selectivity. *Adv. Mater.* **2025**, *37*, e2417994. [CrossRef] [PubMed]
106. Chen, H.; Liu, X.; Gong, D.; Zhu, C.; Liu, G.; Fan, J.; Wu, P.; Li, Z.; Pan, Y.; Shi, G.; et al. Ultrahigh-water-flux desalination on graphdiyne membranes. *Nat. Water* **2023**, *1*, 800–807. [CrossRef]
107. Li, J.; Zhou, K.; Liu, Q.; Tian, B.; Liu, X.; Cao, L.; Cao, H.; Li, G.; Zhang, X.; Han, Y.; et al. Synthesis of two-dimensional ordered graphdiyne membranes for highly efficient and selective water transport. *Nat. Water* **2025**, *3*, 307–318. [CrossRef]
108. Shen, J.; Cai, Y.; Zhang, C.; Wei, W.; Chen, C.; Liu, L.; Yang, K.; Ma, Y.; Wang, Y.; Tseng, C.-C.; et al. Fast water transport and molecular sieving through ultrathin ordered conjugated-polymer-framework membranes. *Nat. Mater.* **2022**, *21*, 1183–1190. [CrossRef]
109. Liu, S.-H.; Shi, W.; Hung, W.-S.; Shi, L.; Xue, B.; She, J.; Song, Z.; Lu, X.; Gray, S.; Lee, K.-R.; et al. Interfacial self-organization of large-area mixed-dimensional polyamide membranes for rapid aqueous nanofiltration. *Nat. Water* **2024**, *2*, 1238–1248. [CrossRef]
110. Yang, H.; Yang, L.; Wang, H.; Xu, Z.; Zhao, Y.; Luo, Y.; Nasir, N.; Song, Y.; Wu, H.; Pan, F.; et al. Covalent organic framework membranes through a mixed-dimensional assembly for molecular separations. *Nat. Commun.* **2019**, *10*, 2101. [CrossRef]
111. Ding, L.; Li, L.; Liu, Y.; Wu, Y.; Lu, Z.; Deng, J.; Wei, Y.; Caro, J.; Wang, H. Effective ion sieving with Ti3C2Tx MXene membranes for production of drinking water from seawater. *Nat. Sustain.* **2020**, *3*, 296–302. [CrossRef]
112. Dang, C.; Helal, A.S.; Zhu, L.; Xu, G.; Zhu, M. Industrial pathways to lithium extraction from seawater: Challenges and perspectives. *Nano Res. Energy* **2023**, *2*, e9120059. [CrossRef]
113. Juve, J.-M.A.; Christensen, F.M.S.; Wang, Y.; Wei, Z. Electrodialysis for metal removal and recovery: A review. *Chem. Eng. J.* **2022**, *435*, 134857. [CrossRef]
114. Li, Y.; Yang, Z.; Yang, K.; Wei, J.; Li, Z.; Ma, C.; Yang, X.; Wang, T.; Zeng, G.; Yu, G.; et al. Removal of chloride from water and wastewater: Removal mechanisms and recent trends. *Sci. Total. Environ.* **2022**, *821*, 153174. [CrossRef] [PubMed]
115. Zhou, Z.; Zhao, K.; Chi, H.-Y.; Shen, Y.; Song, S.; Hsu, K.-J.; Chevalier, M.; Shi, W.; Agrawal, K.V. Electrochemical-repaired porous graphene membranes for precise ion-ion separation. *Nat. Commun.* **2024**, *15*, 4006. [CrossRef]
116. Kitto, D.; Espinoza, C.; Díaz, J.C.; Zamora, J.; Kamcev, J. Fast and selective ion transport in ultrahigh-charge-density membranes. *Nat. Chem. Eng.* **2025**, *2*, 252–260. [CrossRef]
117. Wang, J.; Zhang, Z.; Zhu, J.; Tian, M.; Zheng, S.; Wang, F.; Wang, X.; Wang, L. Ion sieving by a two-dimensional Ti3C2Tx alginate lamellar membrane with stable interlayer spacing. *Nat. Commun.* **2020**, *11*, 3540. [CrossRef]
118. Xu, R.; Yu, H.; Ren, J.; Zhang, W.; Kang, Y.; Wang, Z.; Feng, F.; Xia, X.; Liu, J.Z.; Peng, L.; et al. Regulate Ion Transport in Subnanochannel Membranes by Ion-Pairing. *J. Am. Chem. Soc.* **2025**, *147*, 17144–17151. [CrossRef]
119. Zhang, M.; Zhao, P.; Li, P.; Ji, Y.; Liu, G.; Jin, W. Designing Biomimic Two-Dimensional Ionic Transport Channels for Efficient Ion Sieving. *ACS Nano* **2021**, *15*, 5209–5220. [CrossRef]
120. Guo, L.; Liu, Y.; Zeng, H.; Zhang, S.; Song, R.; Yang, J.; Han, X.; Wang, Y.; Wang, L. Covalently Functionalized Nanopores for Highly Selective Separation of Monovalent Ions. *Adv. Mater.* **2023**, *36*, e2307242. [CrossRef]
121. Qiu, M.; Zhu, Z.; Wang, D.; Xu, Z.; Xia, F.; Jiang, L.; Tian, Y. Superspreading-Confined Assembly of Oriented 2D MOF Membranes for Biomimetic Cation-Regulated Ion Transport. *Adv. Funct. Mater.* **2024**, *34*, 2316040. [CrossRef]
122. Cao, L.; Chen, I.-C.; Li, Z.; Liu, X.; Mubashir, M.; Al Nuaimi, R.; Lai, Z. Switchable Na+ and K+ selectivity in an amino acid functionalized 2D covalent organic framework membrane. *Nat. Commun.* **2022**, *13*, 7894. [CrossRef]
123. Rastgar, M.; Moradi, K.; Burroughs, C.; Hemmati, A.; Hoek, E.; Sadrzadeh, M. Harvesting Blue Energy Based on Salinity and Temperature Gradient: Challenges, Solutions, and Opportunities. *Chem. Rev.* **2023**, *123*, 10156–10205. [CrossRef] [PubMed]
124. Yan, P.; Chen, X.; Liang, Z.; Fang, Y.; Yao, J.; Lu, C.; Cai, Y.; Jiang, L. Two-Dimensional Nanofluidic Membranes with Intercalated In-Plane Shortcuts for High-Performance Blue Energy Harvesting. *Small* **2022**, *19*, e2205003. [CrossRef] [PubMed]
125. Zhi, H.; Yan, P.; Wang, D.; Liu, Y.; Tang, J.; Yang, X.; Liu, Z.; Zhang, Y.; Li, N.; An, M.; et al. Large-Area Graphene-Based Ion-Selective Membranes with Micro/Meso-Pores for Osmotic Energy Harvesting. *Adv. Funct. Mater.* **2024**, *34*, 2401922. [CrossRef]
126. Wang, H.; Su, L.; Yagmurcukardes, M.; Chen, J.; Jiang, Y.; Li, Z.; Quan, A.; Peeters, F.M.; Wang, C.; Geim, A.K.; et al. Blue Energy Conversion from Holey-Graphene-like Membranes with a High Density of Subnanometer Pores. *Nano Lett.* **2020**, *20*, 8634–8639. [CrossRef]
127. Zhu, C.; Liu, P.; Niu, B.; Liu, Y.; Xin, W.; Chen, W.; Kong, X.-Y.; Zhang, Z.; Jiang, L.; Wen, L. Metallic Two-Dimensional MoS_2 Composites as High-Performance Osmotic Energy Conversion Membranes. *J. Am. Chem. Soc.* **2021**, *143*, 1932–1940. [CrossRef]

128. Tong, X.; Liu, S.; Zhao, Y.; Huang, L.; Crittenden, J.; Chen, Y. MXene Composite Membranes with Enhanced Ion Transport and Regulated Ion Selectivity. *Environ. Sci. Technol.* **2022**, *56*, 8964–8974. [CrossRef]
129. Wang, Z.; Zhang, Z.; Qi, H.; Ortega-Guerrero, A.; Wang, L.; Xu, K.; Wang, M.; Park, S.; Hennersdorf, F.; Dianat, A.; et al. On-water surface synthesis of charged two-dimensional polymer single crystals via the irreversible Katritzky reaction. *Nat. Synth.* **2021**, *1*, 69–76. [CrossRef]
130. Zhang, Z.; Bhauriyal, P.; Sahabudeen, H.; Wang, Z.; Liu, X.; Hambsch, M.; Mannsfeld, S.C.B.; Dong, R.; Heine, T.; Feng, X. Cation-selective two-dimensional polyimine membranes for high-performance osmotic energy conversion. *Nat. Commun.* **2022**, *13*, 3935. [CrossRef]
131. Yang, G.; Liu, D.; Chen, C.; Qian, Y.; Su, Y.; Qin, S.; Zhang, L.; Wang, X.; Sun, L.; Lei, W. Stable $Ti_3C_2T_x$ MXene–Boron Nitride Membranes with Low Internal Resistance for Enhanced Salinity Gradient Energy Harvesting. *ACS Nano* **2021**, *15*, 6594–6603. [CrossRef]
132. Duan, R.; Zhou, J.; Ma, X.; Hao, J.; Zhao, D.; Teng, C.; Zhou, Y.; Jiang, L. High Strength MXene/PBONF Heterogeneous Membrane with Excellent Ion Selectivity for Efficient Osmotic Energy Conversion. *Nano Lett.* **2023**, *23*, 11043–11050. [CrossRef] [PubMed]
133. Zhou, J.; Hao, J.; Wu, R.; Su, L.; Wang, J.; Qiu, M.; Bao, B.; Ning, C.; Teng, C.; Zhou, Y.; et al. Maximizing Ion Permselectivity in MXene/MOF Nanofluidic Membranes for High-Efficient Blue Energy Generation. *Adv. Funct. Mater.* **2022**, *32*, 2209767. [CrossRef]
134. Lin, X.; Liu, P.; Xin, W.; Teng, Y.; Chen, J.; Wu, Y.; Zhao, Y.; Kong, X.; Jiang, L.; Wen, L. Heterogeneous MXene/PS-b-P2VP Nanofluidic Membranes with Controllable Ion Transport for Osmotic Energy Conversion. *Adv. Funct. Mater.* **2021**, *31*, 2105013. [CrossRef]
135. Yang, J.; Liu, P.; He, X.; Hou, J.; Feng, Y.; Huang, Z.; Yu, L.; Li, L.; Tang, Z. Photodriven Active Ion Transport Through a Janus Microporous Membrane. *Angew. Chem.* **2020**, *132*, 6303–6307. [CrossRef]
136. Huang, H.; Zhang, X.; Huang, X.; Sun, K.; Chen, S.; Xu, Y.; Xu, F. Synergistic Photoelectric/Photothermal Effects Guided Ion Transport for Enhancing Multiple Climatic Osmotic Energy Conversion Efficiency. *Small* **2025**, *21*, e2500366. [CrossRef]
137. Liu, P.; Zhou, T.; Teng, Y.; Fu, L.; Hu, Y.; Lin, X.; Kong, X.-Y.; Jiang, L.; Wen, L. Light-Induced Heat Driving Active Ion Transport Based on 2D MXene Nanofluids for Enhancing Osmotic Energy Conversion. *CCS Chem.* **2021**, *3*, 1325–1335. [CrossRef]
138. Wang, J.; Song, Z.; He, M.; Qian, Y.; Wang, D.; Cui, Z.; Feng, Y.; Li, S.; Huang, B.; Kong, X.; et al. Light-responsive and ultrapermeable two-dimensional metal-organic framework membrane for efficient ionic energy harvesting. *Nat. Commun.* **2024**, *15*, 2125. [CrossRef]
139. Fan, C.; Zhang, P.; Wang, R.; Xu, Y.; Sun, X.; Zhang, J.; Cheng, J.; Xu, C. Applications of Two Dimensional Material-MXene for Proton Exchange Membrane Fuel Cells (PEMFCs) and Water Electrolysis. *Curr. Nanosci.* **2021**, *17*, 2–13. [CrossRef]
140. Ye, C.; Wang, A.; Breakwell, C.; Tan, R.; Bezzu, C.G.; Hunter-Sellars, E.; Williams, D.R.; Brandon, N.P.; Klusener, P.A.A.; Kucernak, A.R.; et al. Development of efficient aqueous organic redox flow batteries using ion-sieving sulfonated polymer membranes. *Nat. Commun.* **2022**, *13*, 3184. [CrossRef]
141. Sun, P.Z.; Yang, Q.; Kuang, W.J.; Stebunov, Y.V.; Xiong, W.Q.; Yu, J.; Nair, R.R.; Katsnelson, M.I.; Yuan, S.J.; Grigorieva, I.V.; et al. Limits on gas impermeability of graphene. *Nature* **2020**, *579*, 229–232. [CrossRef]
142. Griffin, E.; Mogg, L.; Hao, G.-P.; Kalon, G.; Bacaksiz, C.; Lopez-Polin, G.; Zhou, T.; Guarochico, V.; Cai, J.; Neumann, C.; et al. Proton and Li-Ion Permeation through Graphene with Eight-Atom-Ring Defects. *ACS Nano* **2020**, *14*, 7280–7286. [CrossRef] [PubMed]
143. Zeng, Z.; Song, R.; Zhang, S.; Han, X.; Zhu, Z.; Chen, X.; Wang, L. Biomimetic N-Doped Graphene Membrane for Proton Exchange Membranes. *Nano Lett.* **2021**, *21*, 4314–4319. [CrossRef] [PubMed]
144. Ji, Y.; Hao, G.-P.; Tan, Y.-T.; Xiong, W.; Liu, Y.; Zhou, W.; Tang, D.-M.; Ma, R.; Yuan, S.; Sasaki, T.; et al. High proton conductivity through angstrom-porous titania. *Nat. Commun.* **2024**, *15*, 10546. [CrossRef] [PubMed]
145. Mogg, L.; Hao, G.-P.; Zhang, S.; Bacaksiz, C.; Zou, Y.-C.; Haigh, S.J.; Peeters, F.M.; Geim, A.K.; Lozada-Hidalgo, M. Atomically thin micas as proton-conducting membranes. *Nat. Nanotechnol.* **2019**, *14*, 962–966. [CrossRef]
146. Li, J.; Cao, H.; Wang, Q.; Zhang, H.; Liu, Q.; Chen, C.; Shi, Z.; Li, G.; Kong, Y.; Cai, Y.; et al. Space-Confined Synthesis of Monolayer Graphdiyne in MXene Interlayer. *Adv. Mater.* **2023**, *36*, e2308429. [CrossRef]
147. Li, J.; Wang, C.; Su, J.; Liu, Z.; Fan, H.; Wang, C.; Li, Y.; He, Y.; Chen, N.; Cao, J.; et al. Observing Proton–Electron Mixed Conductivity in Graphdiyne. *Adv. Mater.* **2024**, *36*, e2400950. [CrossRef]
148. Xu, J.; Jiang, H.; Shen, Y.; Li, X.-Z.; Wang, E.G.; Meng, S. Transparent proton transport through a two-dimensional nanomesh material. *Nat. Commun.* **2019**, *10*, 3971. [CrossRef]
149. Li, W.; Xu, C.; Xiong, T.; Jiang, Y.; Ma, W.; Yu, P.; Mao, L. Giant Water Uptake Enabled Ultrahigh Proton Conductivity of Graphdiyne Oxide. *Angew. Chem. Int. Ed. Engl.* **2022**, *62*, e202216530. [CrossRef]
150. Chakraborty, G.; Park, I.-H.; Medishetty, R.; Vittal, J.J. Two-Dimensional Metal-Organic Framework Materials: Synthesis, Structures, Properties and Applications. *Chem. Rev.* **2021**, *121*, 3751–3891. [CrossRef]
151. Shi, B.; Pang, X.; Li, S.; Wu, H.; Shen, J.; Wang, X.; Fan, C.; Cao, L.; Zhu, T.; Qiu, M.; et al. Short hydrogen-bond network confined on COF surfaces enables ultrahigh proton conductivity. *Nat. Commun.* **2022**, *13*, 6666. [CrossRef]

152. Wang, X.; Shi, B.; Yang, H.; Guan, J.; Liang, X.; Fan, C.; You, X.; Wang, Y.; Zhang, Z.; Wu, H.; et al. Assembling covalent organic framework membranes with superior ion exchange capacity. *Nat. Commun.* **2022**, *13*, 1020. [CrossRef] [PubMed]
153. Guo, R.; Zhou, Y.; Wang, W.; Zhai, Y.; Liu, X.; He, W.; Ou, W.; Ding, R.; Zhang, H.-L.; Wu, M.; et al. Interlayer confinement toward short hydrogen bond network construction for fast hydroxide transport. *Sci. Adv.* **2025**, *11*, eadr5374. [CrossRef] [PubMed]
154. Asghar, M.R.; Zhang, W.; Su, H.; Zhang, J.; Liu, H.; Xing, L.; Yan, X.; Xu, Q. A review of proton exchange membranes modified with inorganic nanomaterials for fuel cells. *Energy Adv.* **2024**, *4*, 185–223. [CrossRef]
155. Radenahmad, N.; Afif, A.; Petra, P.I.; Rahman, S.M.; Eriksson, S.-G.; Azad, A.K. Proton-conducting electrolytes for direct methanol and direct urea fuel cells—A state-of-the-art review. *Renew. Sustain. Energy Rev.* **2016**, *57*, 1347–1358. [CrossRef]
156. Wang, F.; Zuo, Z.; Li, L.; Li, K.; He, F.; Jiang, Z.; Li, Y. Large-Area Aminated-Graphdiyne Thin Films for Direct Methanol Fuel Cells. *Angew. Chem.* **2019**, *131*, 15152–15157. [CrossRef]
157. Li, L.; Zuo, Z.; He, F.; Jiang, Z.; Li, Y. Nitrogen-rich Graphdiyne Film for Efficiently Suppressing the Methanol Crossover in Direct Methanol Fuel Cells. *Chem. Res. Chin. Univ.* **2021**, *37*, 1275–1282. [CrossRef]
158. Tempelman, C.; Jacobs, J.; Balzer, R.; Degirmenci, V. Membranes for all vanadium redox flow batteries. *J. Energy Storage* **2020**, *32*, 101745. [CrossRef]
159. Kim, S.; Choi, J.; Choi, C.; Heo, J.; Kim, D.W.; Lee, J.Y.; Hong, Y.T.; Jung, H.-T.; Kim, H.-T. Pore-Size-Tuned Graphene Oxide Frameworks as Ion-Selective and Protective Layers on Hydrocarbon Membranes for Vanadium Redox-Flow Batteries. *Nano Lett.* **2018**, *18*, 3962–3968. [CrossRef]
160. Di, M.; Xiu, Y.; Dong, Z.; Hu, L.; Gao, L.; Dai, Y.; Yan, X.; Zhang, N.; Pan, Y.; Jiang, X.; et al. Two-dimensional MoS2 nanosheets constructing highly ion-selective composite membrane for vanadium redox flow battery. *J. Membr. Sci.* **2021**, *623*, 119051. [CrossRef]
161. Pang, B.; Du, R.; Chen, W.; Cui, F.; Wang, N.; Zhao, H.; Xie, G.; Tiantian, L.; He, G.; Wu, X. Self-supporting sulfonated covalent organic framework as a highly selective continuous membrane for vanadium flow battery. *Energy Storage Mater.* **2024**, *67*, 103293. [CrossRef]

Disclaimer/Publisher's Note: The statements, opinions and data contained in all publications are solely those of the individual author(s) and contributor(s) and not of MDPI and/or the editor(s). MDPI and/or the editor(s) disclaim responsibility for any injury to people or property resulting from any ideas, methods, instructions or products referred to in the content.